

Spectroscopic measurements and models of energy deposition in the substrate of quantum circuits by natural ionizing radiation

Joseph W. Fowler,^{1,2,*} Paul Szypryt,^{1,2} Raymond Bunker,³ Ellen R. Edwards,³ Ian Fogarty Florang,^{2,1} Jiansong Gao,^{1,†} Andrea Giachero,^{2,1,4} Shannon F. Hoogerheide,⁵ Ben Loer,³ H. Pieter Mumm,⁵ Nathan Nakamura,^{1,2} Galen C. O’Neil,¹ John L. Orrell,³ Elizabeth M. Scott,⁶ Jason Stevens,^{1,2} Daniel S. Swetz,¹ Brent A. VanDevender,³ Michael Vissers,¹ and Joel N. Ullom^{1,2}

¹*Quantum Sensors Division, National Institute of Standards and Technology, 325 Broadway, Boulder, Colorado USA 80305*

²*Department of Physics, University of Colorado, Boulder, Colorado USA 80309*

³*Pacific Northwest National Laboratory, Richland, Washington USA 99354*

⁴*Department of Physics, University of Milano-Bicocca, Milan, Italy*

⁵*Radiation Physics Division, National Institute of Standards and Technology, 100 Bureau Drive, Gaithersburg, Maryland USA 20899*

⁶*Department of Physics, Centre College, 600 West Walnut Street, Danville, Kentucky USA 40422*

(Dated: April 18, 2024)

Naturally occurring background radiation is a potential source of correlated decoherence events in superconducting qubits that will challenge error-correction schemes. To characterize the radiation environment in an unshielded laboratory, we performed broadband, spectroscopic measurements of background events in silicon substrates located inside a millikelvin refrigerator, an environment representative of superconducting qubit systems. We measured the background spectra in silicon substrates of two thicknesses, 500 μm and 1500 μm , and obtained the average event rate and the integrated power deposition. In a 25 mm^2 area and the thinner substrate, these values are 0.023 events per second and 4.9 keV s^{-1} , respectively, counting events that deposit at least 40 keV. We find that the spectrum of background events is nearly featureless, and its intensity decreases by a factor of 40 000 between 100 keV and 3 MeV for silicon substrates 500 μm thick. We find the cryogenic measurements to be in good agreement with predictions based on simple measurements of the terrestrial gamma-ray flux outside the refrigerator, published models of cosmic-ray fluxes, a crude model of the cryostat, and radiation-transport simulations. No free parameters are required to predict the background spectra in the silicon substrates. The good agreement between measurements and predictions allows confident assessment of the relative contributions of terrestrial and cosmic background sources and their dependence on substrate thickness. Our spectroscopic measurements are performed with superconducting microresonators located on micromachined silicon islands that define the interaction volume with background radiation. The resonators transduce deposited energy to a readily detectable electrical signal. Microresonator readout closely resembles dispersive superconducting qubit readout, so similar devices—with or without micromachined islands—are suitable for integration with superconducting quantum circuits as detectors for background events. We find in our specific laboratory conditions that gamma-ray emissions from radioisotopes are responsible for the majority of events depositing $E < 1.5 \text{ MeV}$, while nucleons among the cosmic-ray secondary particles cause most events that deposit more energy. These results suggest several paths to reducing the impact of background radiation on quantum circuits.

Keywords: Superconducting devices and qubits; Interactions of radiation with matter; Thermal kinetic inductance detectors

I. INTRODUCTION

There is at present widespread interest in developing quantum computers that use qubits based on a variety of physical systems, including systems in which the qubits are deposited on or in silicon substrates. Here we focus on superconducting qubits [1, 2] although some spin-based qubits also use silicon substrates [3]. Many improvements are needed to realize a practical and useful quantum computer, including improving the coherence of individual qubits. Naturally occurring background radiation is

a potential source of decoherence that will be present even in qubits that are themselves perfect. Sources of background radiation include energetic charged particles and gamma rays created by the interaction of cosmic rays with the Earth’s atmosphere. The decay of ubiquitous terrestrial radioisotopes is another source, producing gamma rays and alpha and beta particles. Techniques have been developed to reduce radiation backgrounds, but these are often extreme in nature. They include conducting experiments deep underground to attenuate cosmic radiation sources, using massive shields to attenuate terrestrial gamma rays, and constructing experiments exclusively from materials with high radiopurity. Given how difficult, costly, and inconvenient it can be to implement these techniques, it is likely that future quantum computers must be robust to the radiation back-

* Corresponding author: Joe.Fowler@nist.gov

† Currently at Amazon Web Services Center for Quantum Computing, Pasadena, California USA

grounds found in conventional laboratories. As a result, it is important to measure and understand the intensity and spectral distribution of background radiation events that future quantum circuits will encounter. Modeling these backgrounds is possible, but the most reliable simulations are those validated by measurements.

A superconducting quantum circuit consists of metal and dielectric films deposited and patterned on a piece of silicon with planar dimensions near 1 cm^2 . The films for a single qubit typically occupy only a small fraction of the area of the substrate, and their thickness is typically hundreds of nanometers, at most, while the substrate is generally one thousand times thicker. Incident radiation is far more likely to interact with the comparatively massive substrate than it is to interact directly with the films of the circuit. Energy deposited in the substrate will propagate within it as phonons, and to a lesser extent as charge. Some of these excitations will interact with the films on the substrate surface. Such interactions can create quasiparticles in a superconductor, cause decoherence in a qubit, or have other unwelcome effects on circuit performance [4–6]. Measurements of the background event rate, event spectrum, and integrated power as a function of substrate dimensions are needed to validate models and ultimately to understand the impact of background radiation. The fraction of the energy deposited in the substrate by a background event that the surface films ultimately absorb is also of interest, as are the effects of this energy on circuit performance. Because these consequences depend strongly on the details of the circuit design, they are not discussed here. This report focuses on results that generalize readily: the interaction of background radiation events with silicon substrates.

Naturally occurring ionizing radiation has been suggested as a source of the excess quasiparticle population observed in qubits [4, 5], as well as in other superconducting devices [7]. The same work showed that ionizing radiation limited the coherence time of the qubits under study to a few milliseconds and that use of a gamma-ray shield produced a small improvement in coherence. Ionizing radiation has also been shown to produce transient events in superconducting microresonators [8]. When the same devices were operated underground to shield against cosmic rays, the event rate was reduced by a factor of 30 and the quality factor of the resonators improved by a factor of four. Other authors [5, 9] operating circuits with several qubits on the same substrate have observed “error bursts,” in which the coherence of multiple qubits is simultaneously disrupted, even qubits separated by millimeters. These error bursts reveal both the danger to error correction schemes and the likelihood of the root cause being energy deposition in the shared substrate. Various techniques have been proposed or demonstrated to reduce the energy that propagates to a thin-film circuit from radiation interactions in the supporting substrate [6, 10, 11]. Despite this growing body of literature, which includes simulations of the expected spectrum of substrate events due to background radiation [8, 9], this

spectrum has not previously been measured. Yet, its details are important for the development of schemes to protect qubits from background radiation, and for understanding the likely limits of such efforts.

In a superconducting quantum processor, the silicon substrate hosting the qubits is enclosed in several layers of metal packaging within a millikelvin refrigeration system. The inner-most metal enclosure is typically at a temperature near 10 mK and consists of a connectorized copper box. The silicon substrate is mounted to the inside of the box via an adhesive and/or pressure contacts such as mechanical clips. Electrical signals are carried between the connectors and the substrate by circuit boards and/or fan-out chips, and wire bonds or bump bonds provide electrical and thermal connections between the substrate and the rest of the package. This multi-component assembly represents a large target for background radiation. The high specific heat of the unpaired electrons in the normal metal components (such as the copper enclosure) and their strong thermal connection to the cooling source of the refrigerator mean that energy deposited in the metal enclosure is rapidly thermalized and removed. Nonetheless, there are other pathways for background radiation that originates in or interacts with the substrate packaging to excite the substrate. The decay products from radio-impurities located very near the substrate are a potential source of background events, as are secondary particles or photons produced by interactions of higher energy particles or photons [12]. However, we will show that in a conventional laboratory environment, these effects are less important than events caused by the interaction of background radiation with the circuit substrate itself.

While there has been extensive prior work on characterizing natural radiation backgrounds, the topic is sufficiently broad and complex that a simple description of likely radiation backgrounds is not readily available to the quantum information science (QIS) community. Radiation described as “cosmic rays” has contributions from muons, electrons, protons, neutrons, and gamma rays. Several cosmic-ray models are available to the interested user; the predictions of the models vary somewhat, and fluxes depend strongly on altitude and weakly on additional factors such as weather, geomagnetic latitude, and solar activity. Radiation from terrestrial radioisotopes potentially depends on the local geology and the composition of nearby construction. Even with perfect knowledge of the radiation sources outside a cryostat containing a quantum circuit, the effects of that radiation on the circuit substrate require propagation and interaction calculations that depend on the type of radiation and the detailed geometry. Hence, an important contribution of this work is providing the reader with a clear description of how we determined the radiation background in our laboratory that can be adapted to their own.

Another contribution of this work is the validation of the background model with spectroscopic measurements of the radiation background in silicon substrates that

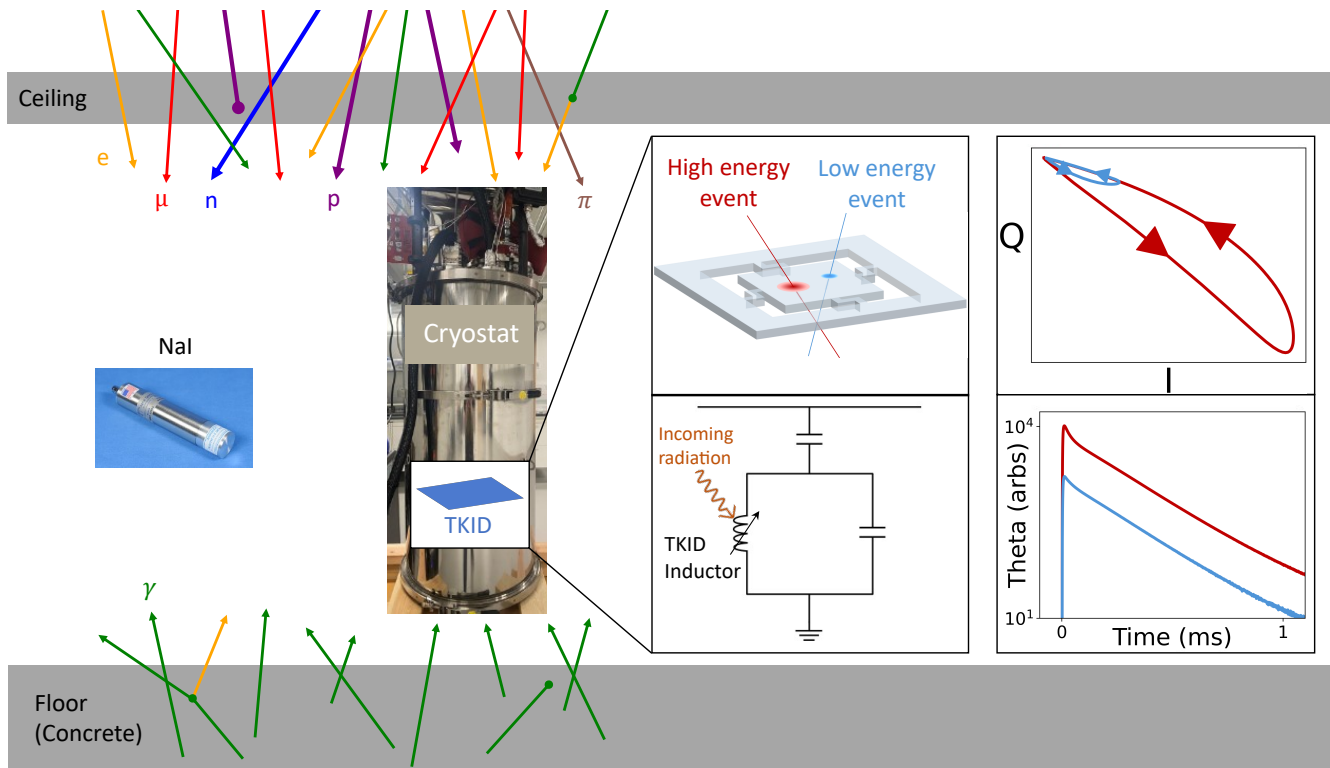


FIG. 1. Overview of the measurements made in this work. A superconducting spectroscopic sensor on a silicon substrate (TKID) is operated inside a millikelvin cryostat. The TKID acts as a radiation-sensitive inductor in a resonant circuit. Cosmic rays of many particle species arrive from above, screened only partially by the concrete ceiling. Radioisotopes in or beneath the floor emit gamma rays (and the occasional Compton-scattered electron). Heating of the TKID by absorbed radiation causes transient changes in the resonator’s complex RF transmission, returning to the resting value in an approximately exponential “pulse.” A conventional NaI detector is used to measure the intensity of both sources outside the cryostat, after which the spectrum of energy deposited in the silicon TKID can be modeled.

are representative of quantum circuits (Figure 1). Comparable validation has not been performed before, because few energy-resolving radiation detectors sensitive over the relevant energy range are also similar in size and composition to qubit circuits. As we will show, the background spectrum depends strongly on the size of the interaction volume. The background spectrum measured by a conventional radiation detector with dimensions of ~ 100 mm differs substantially from the spectrum in a silicon substrate less than 1 mm thick; using the former to predict the latter without validation would be a significant analytical leap.

II. TERRESTRIAL RADIATION BACKGROUNDS

The primary sources of ionizing radiation that penetrate a cryostat in a typical laboratory are the various species of secondary cosmic rays and the gamma radiation that accompanies the decay of common radioactive isotopes. We call these the cosmic-ray and terrestrial radiation backgrounds, respectively. The terrestrial background creates the majority of the interaction events and

of the total energy deposited in millimeter-scale silicon devices in a typical laboratory environment, while cosmic rays are responsible for the rarer events that deposit the largest energies. We model the terrestrial radiation in this section and the cosmic rays in Section III.

Some sources of background radiation are subdominant in an unshielded, ground-level laboratory and need not be modeled. Events caused by interactions of decay products from most radio-impurities in the experimental setup (e.g., the dilution refrigerator and the qubit packaging) are expected to be much less frequent than events from external sources [13]. Potential exceptions are alpha emission from materials with a direct line-of-sight to the surface of the cryogenic circuit, which could contribute significantly. We have alpha-counted those materials with the largest line-of-sight solid angle to the circuit: the copper and aluminum lids of the housing, and the substrate itself. The measured rates were below the alpha counter’s intrinsic background, corresponding to levels well below the rates of external sources. Although the radiopurity of the experimental materials may ultimately be important for highly shielded quantum circuits, we concluded that it is not a critical consideration for the present measurement. There are also external

sources of alpha and beta radiation (along with gammas), but we also ignore these charged-particle backgrounds on the basis that metallic packaging and a cryostat’s vacuum shells effectively shield the cryogenic circuit from such radiation.

For the purposes of modeling radiation backgrounds, we assume two example silicon substrates 5 mm square, 500 μm and 1500 μm thick, with a thin superconducting circuit fabricated on one surface of each. These sizes correspond to the specific silicon microcalorimeters we used for the present measurements (Section IV), and more generally to the size, shape, and composition of a typical superconducting qubit. While few qubits might use substrates as thick as 1500 μm , this size offers us the chance to check how backgrounds scale with wafer thickness.

A. Three predominant radioactive decay chains

Trace levels of many naturally occurring radioactive materials are present in a typical laboratory; they are found in structural materials such as concrete and in the underlying soil and rock [14, 15]. The gamma-ray spectrum emitted by these natural radiation sources consists of hundreds of distinct emission energies. The most common emitters include the primordial isotopes ^{40}K , ^{232}Th , and ^{238}U , whose lifetimes are all long enough that they survive today from the time of the Earth’s formation. ^{40}K decays to ^{40}Ar by electron capture with 11 % probability, emitting a 1.461 MeV gamma ray. Thorium and uranium give rise to two lengthy decay chains. The thorium chain includes twelve distinct decays, accompanied by both x-ray and gamma-ray emissions with energies as high as 2.615 MeV. We model this chain by the 289 emissions with energies of at least 50 keV and emitted by at least 0.01 % of the decays of either thorium or its progeny. The uranium chain includes the decays of eighteen radioisotopes, yielding 246 gamma-ray and 33 x-ray emissions above 50 keV and 0.01 % probability. [16] All of these the gamma-ray and x-ray emissions appear as distinctive “lines” in the response spectrum of typical gamma-ray instruments.

The spectrum incident on a quantum circuit, however, is not composed only of these distinct lines. A prominent continuum is also present, the result of gammas that have undergone Compton scattering before reaching the substrate. To model this energy-loss mechanism and the ejected energetic electrons, we used the GEANT4 particle-transport Monte Carlo code [17–19], as driven by the Tool for Particle Simulation (TOPAS) [20, 21]. We assume that the emitters are uniformly distributed throughout a slab of concrete 22 cm thick. We treat this as an approximation for any realistic foundation under a laboratory building and for the underlying rock. The attenuation length in concrete for all gamma rays of interest (that is, energies no higher than 2.615 MeV) is 11 cm or less, so we consider a 22 cm-thick distribution to be a useful proxy for the full thickness of the Earth’s crust.

This modeling approximation is thin enough to permit efficient simulations, yet thick enough to capture the energy distribution of photons emitted at a realistic range of depths in a dense material.

We fit models of the complex terrestrial gamma spectrum to measurements with only five intensity parameters. To achieve this simplification, we assume secular equilibrium among the isotopes within a given decay chain. That is, we take the relative proportions of isotopes in a chain to be constant, the result of an equilibrium between production and decay of each radioisotope but the first. Secular equilibrium is anticipated in natural materials, in the absence of chemical processing. One potential exception arises from the gaseous nature of radon: it could be enhanced or depleted in a material by mechanical means alone, so its production and decay need not be locally in equilibrium. Thus, we model the terrestrial background with one ^{40}K intensity, plus potentially distinct intensities of the “pre-radon” and “post-radon” segments of the ^{232}Th and ^{238}U decay chains: a total of five parameters. In practice, our measurements set no meaningful constraints on the pre-radon segment of the uranium chain.

B. Gamma-ray measurements with a scintillating-crystal spectrometer

We have estimated the five unknown activities of the terrestrial-gamma model from spectroscopic measurements. For this purpose, we used a commercial gamma-ray detector, consisting of a scintillating NaI crystal mated to a photomultiplier tube. The NaI crystal was a cylinder 76.2 mm long and 76.2 mm in diameter. The gain scale was calibrated from the two most prominent gamma-ray peaks, those due to ^{40}K and ^{208}Tl at 1.461 MeV and 2.615 MeV. The measurement was repeated at four laboratories in one building at the National Institute of Standards and Technology (NIST) labs in Boulder, Colorado, with similar results. Two other measurements made in a newer building on the NIST site and at the Pacific Northwest National Laboratory in Richland, Washington showed lower overall intensities but an otherwise similar spectrum (Supplemental Material: Figure A.1). At each location, measurements were made in both a high-gain mode (for detection of terrestrial gamma rays) and a low-gain mode (for cosmic rays). The highest detected energies in these modes were approximately 4 MeV and 75 MeV, respectively.

The high-gain spectra are described well by the combination of lines and continuum gamma rays from the dominant decay chains. The five activities were fit under the assumption that the NaI spectrometer has a purely Gaussian energy-resolving function with resolution scaling as $\sigma(E) = A\sqrt{E}$. A small contribution from cosmic rays was estimated based on the low-gain measurements (Section III) and fixed during the fit. The energy calibration was performed on the measured spectrum be-

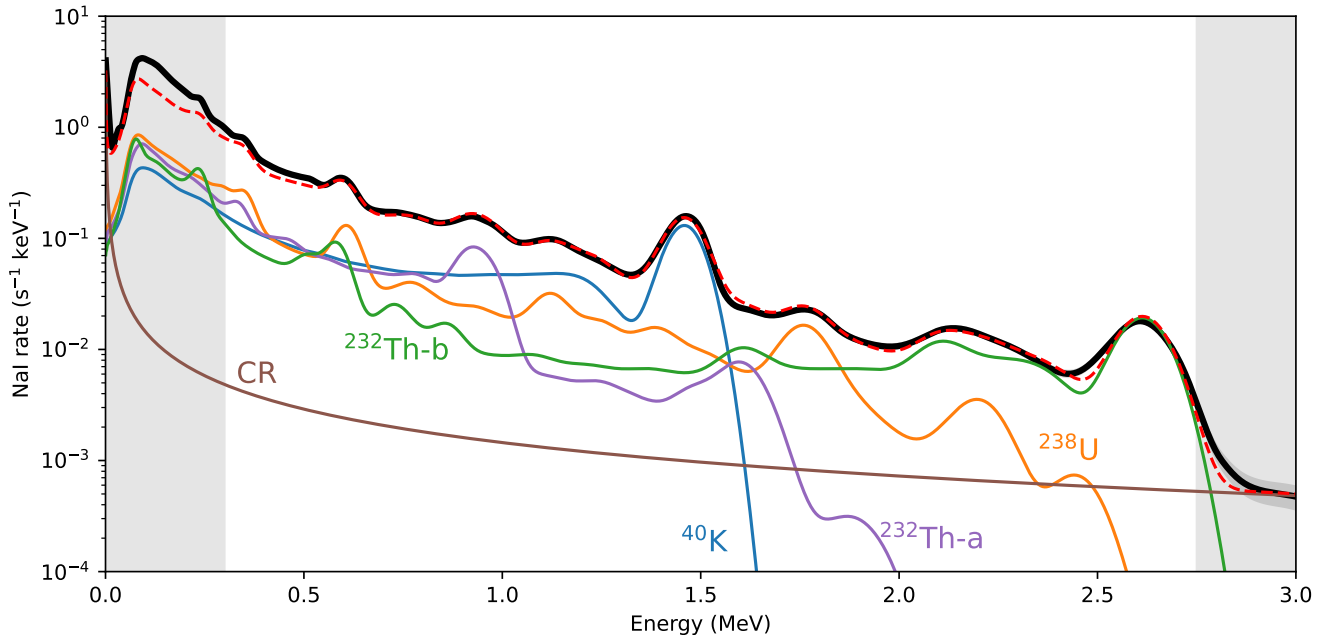


FIG. 2. The reference gamma-ray background spectrum measured with the NaI scintillator (solid black) and the model of the same (dashed red). The model is the sum of the computed spectrum produced by cosmic rays (CR) plus each of the three indicated radioactive decay chains (^{40}K , ^{232}Th , and ^{238}U). The Th chain is further divided into pre- and post-radon segments, labeled $^{232}\text{Th-a}$ and $^{232}\text{Th-b}$, which are not assumed to be in secular equilibrium with each other. The model was fit to the data between 0.3 MeV and 2.75 MeV (i.e., excluding the shaded areas at the left and right of the figure) with the activity of the four decay chain segments allowed to vary. The cosmic-ray level was fixed by measurements at higher energy (Section III).

fore fitting for activities, so the free parameters of the fit are the five activities (one for each decay-chain segment) and the scale of the energy resolution, A . The best-fit A corresponds to 100 keV resolution (FWHM) at 1000 keV. Uncertainties in the measured spectrum are assumed to be dominated by Poisson (counting) statistics.

The data prove to be insensitive to the activity of the pre-radon segment of the ^{238}U chain, which generates relatively few gamma rays. Therefore, we make the simplifying assumption that the entire ^{238}U chain is in secular equilibrium and repeat the fit with only four unknown activities. Figure 2 compares the best-fit model and its components with the reference measurement. The agreement is good, though not consistent with purely statistical deviations: the model under-predicts the measured flux below 0.5 MeV and seems to underestimate the energy resolution at the ^{208}Tl peak (2.615 MeV). The statistical uncertainties are approximately 1% of the activity values (or 0.3% for the $^{232}\text{Th-b}$ chain). The systematic dependence on details of the fitting procedure is larger, $\sim 5\%$.

We use the NaI-based reference measurement to determine the absolute activity of the three decay chains (Table I for the reference laboratory). Significant variation between locations is expected and observed. Measurements made in different buildings (Supplemental Material Figure A.1) showed lower absolute activities than our

Isotope	Specific activity (Bq kg^{-1})	γ escape rate ($\text{cm}^{-2} \text{s}^{-1}$)
^{40}K	1030	1.5
^{238}U chain	76	1.8
$^{232}\text{Th-a}$ chain	126	1.6
$^{232}\text{Th-b}$ chain	82	1.4

TABLE I. Specific activities determined from NaI scintillator measurements in the reference laboratory. For decay chains, the specific activity is that of the parent isotope; its progeny are assumed to be in secular equilibrium. The $^{232}\text{Th-a}$ and $^{232}\text{Th-b}$ activity values refer to the pre-radon and post-radon segments of the decay chain. Emitters are assumed to be uniformly distributed through a concrete layer 22 cm thick. The γ escape rate is the rate per unit area of photons escaping the upper surface of the floor, after substantial attenuation in the concrete slab (approximately 20 gamma rays escape the top surface for every 100 emitted in the slab). The values are subject to uncertainties of approximately 1% (statistical) and 5% (systematic).

reference measurement, by factors of 2.5 and 4. Widely varying radio-isotope activity levels are the natural result of construction with different concrete and flooring materials. The activity levels in the reference lab are marginally higher than typical for concrete samples but well within the range of natural activities observed in building materials [14, 22].

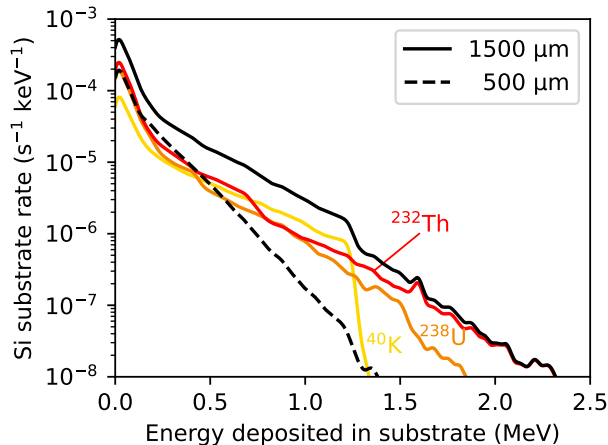


FIG. 3. Predicted spectrum of energy deposited by terrestrial gamma-ray sources in a silicon substrate, $5 \times 5 \text{ mm}^2$ square and $1500 \mu\text{m}$ or $500 \mu\text{m}$ thick. The three colored curves labeled by decay chain show the contributions of each to the spectrum for the thicker substrate.

C. Terrestrial backgrounds in silicon substrates

Given these detector-independent activity values, we used TOPAS and GEANT4 to model the spectrum of energy that would be deposited in the $5 \text{ mm} \times 5 \text{ mm}$ silicon substrate of a quantum circuit after propagation through the cryostat. Figure 3 shows the prediction for two substrate thicknesses ($500 \mu\text{m}$ and $1500 \mu\text{m}$), as well as the breakdown of one spectrum into the contributions from the different terrestrial sources. These predictions assume the activity level found in our reference measurement; the measurements made in several other locations demonstrate that the overall level can vary by factors of a few from one laboratory to another.

While we model the complete spectrum, and eventually compare it to measurement (Section VI), we also find the rate of interactions and the rate of energy deposition in the substrate to be efficient summaries of the spectrum. The predicted interaction rates for terrestrial gamma rays to deposit more than 40 keV in the silicon substrates are 0.0153 and 0.038 events per second for wafers of thickness $500 \mu\text{m}$ and $1500 \mu\text{m}$, respectively. Energy is deposited at corresponding rates of 2.98 keVs^{-1} and 8.3 keVs^{-1} . These values have relative systematic uncertainties of $\pm 5\%$ due to limitations of the simplified model. The statistical uncertainties are smaller, 1% . The cutoff of 40 keV is chosen because the imperfect thermal isolation of our devices confuses measurement at lower energies (see Section V).

The energy deposition rates are in a ratio of 2.8. Without the 40 keV cutoff, the ratio becomes 3.1. Thus the power deposited in the silicon is approximately proportional to the ratio of volumes, as expected. The predicted interaction rate is only 2.5 times larger in the thicker

wafer, however. As discussed in Section VII, the rate of gamma rays interacting directly in the silicon is indeed in the expected 3:1 ratio. Secondary electrons created by Compton scattering of gamma rays in material around the silicon, on the other hand, interact readily with even very thin silicon substrates, in a rate proportional not to the silicon volume but the (effective) area. The electrons therefore increase the total interaction rate in substrates of any thickness by similar amounts, and reduce the ratio.

III. COSMIC-RAY BACKGROUNDS

A. Modeling the cosmic rays

Primary cosmic rays—for the most part protons or other fully ionized nuclei—enter the Earth’s atmosphere and interact high in the stratosphere with the nucleus of an air molecule. These relativistic collisions produce a spray of nuclear material which can induce further collisions in a growing particle population known as a cosmic-ray air shower [23, 24]. The secondary cosmic rays in the air shower that reach the ground consist of a diverse assortment of particle types, which are responsible for the cosmic-ray background observed in a laboratory and relevant to QIS instruments. These secondaries include muons and electrons of either charge, protons, neutrons, and gamma rays. Even highly unstable particles such as pions appear in very small numbers. We find that terrestrial gamma rays exceed the cosmic-ray background in terms of event rate and power deposition in a silicon substrate in our laboratory, though the protons and neutrons in cosmic rays are responsible for essentially all events in which at least 2 MeV is deposited.

Many models of the cosmic-ray spectrum are available in the literature. Some describe the spectra of all particle types, while others are restricted to muons, the most penetrating species. Some parameterize the results of air-shower simulations; others represent a purely empirical synthesis of cosmic-ray measurements. Wanting to model all particles (and not only muons), we chose to use the PARMA 4.0 tool [25], an analytical approximation of radiation in the atmosphere. PARMA parameterizes the distribution of energies and zenith angles expected for each of several particle types, at the elevation (or atmospheric depth) of the user’s choice. The parameters are fitted to match the results of air-shower simulations performed with the Particle and Heavy Ion Transport System (PHITS) [26].

As with the terrestrial gamma rays, we use TOPAS and GEANT4 to model the transport and interactions of the cosmic rays with shielding and detectors. We created an intermediate tool, `MuscRat.jl` [27], to generate millions of random cosmic rays by sampling from the distributions PARMA produced. These cosmic rays’ particle species and their position and momentum vectors were stored as phase-space files, an input data format supported by TOPAS.

The GEANT4 particle-transport framework is readily integrated with a different cosmic-ray generator called CRY [28]. CRY has been found to under-predict the intensity of near-horizontal muons [29], so we used the CRY+GEANT4 combination only as a check on our models. We did not ultimately find any meaningful differences between the predictions when cosmic-ray secondaries were generated by CRY versus PARMA. We preferred PARMA as our cosmic-ray generator mainly because it predicts distributions at arbitrary elevation or atmospheric depth (CRY works at only three specific elevations), and it is flexible enough to fit readily into our modeling tool chain.

Our cosmic-ray models include the shielding effect of a concrete ceiling 18 cm thick (a value found in building blueprints), as well as the cryostat (here approximated by a simple planar layer of aluminum 1 cm thick). These materials reduce the energy carried by muons by only 2.4%. They also convert a portion of the energy carried by gamma rays into energetic electrons and positrons. The ceiling also reduces the energy carried by neutrons and protons, by approximately 30%. Because it preferentially attenuates the nucleons of lower energy, which deposit energy more efficiently in a thin object like a silicon wafer, the ceiling and cryostat reduce the rate of rare events in the high-energy end of the spectrum expected in a silicon substrate by a factor of approximately 3 (Supplementary Material Figure A.3). Overall, however, in an above-ground laboratory, the ceiling and cryostat body produce only a small reduction in the cosmic-ray rate and a modest redistribution of energy among particle species.

B. Cosmic-ray measurements with a scintillating-crystal spectrometer

To test the cosmic-ray models, we measured the background spectrum with the same NaI scintillator described in Section II B. When configured in a low-gain mode, the spectrometer could measure energetic events up to approximately 75 MeV. This energy range is well matched to the energy loss of minimum-ionizing particles in NaI along the possible geometric paths through the cylindrical NaI crystal with length and diameter both 76.2 mm. The typical path produces a broad energy-loss peak centered between 30 MeV and 40 MeV. As with the measurements of terrestrial gammas, we repeated the cosmic-ray measurements in multiple buildings at two sites. One site was near sea level, while the Boulder, Colorado measurements were performed at 1460 m above sea level (mean atmospheric depth 860 g cm⁻²). The observed cosmic-ray flux is approximately 33% higher at the higher elevation, consistent with predictions of the PARMA model.

We observed a clear difference between the energy spectrum of cosmic-ray events depending upon whether the NaI cylinder's axis was oriented vertically or horizontally. Because cosmic rays are not isotropic, the distribution of geometric paths through a cylinder is different in

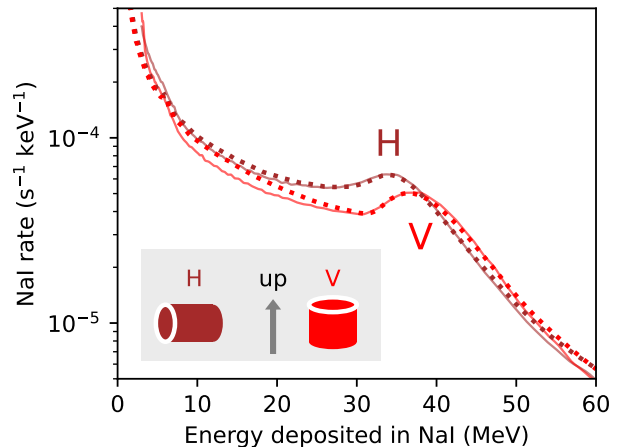


FIG. 4. Cosmic-ray spectra measured by a NaI scintillator in neighboring labs (solid lines), one with the crystal cylinder oriented vertically (V), the other horizontally (H). The gray inset indicates the orientation conventions. TOPAS+GEANT4 models of the detector in each orientation are shown as dotted lines. The models are scaled in intensity by a factor of 0.88 relative to the PARMA output to agree with the measurement. The energy scale is fixed by calibration to terrestrial gamma-ray features at 1.4 MeV and 2.7 MeV then fit to permit a slightly nonlinear response by pinning the peaks at the expected energies of 34 MeV and 37 MeV. The nonlinearity is found to be a 1% effect at these higher energies.

the two orientations. Measurements and model predictions exhibit an identical dependence on cylinder orientation (Figure 4). The most probable energy loss is 34 MeV for a horizontal cylinder and 37 MeV for a vertical one. The mean count rate and rate of energy deposition are equal in the two orientations. This observation supports the validity of the particle-transport modeling.

The NaI measurements constrain the intensity of the cosmic rays. The NaI spectra shown in Figure 4, as well as the other four measured at the Boulder site, all agree that the cosmic-ray rate was somewhat lower than predicted by PARMA. To achieve a good fit of the model to the measurements, it was necessary to scale the μ^\pm intensity separately from the other electromagnetic components (e^\pm and γ). The hadronic particles (protons, neutrons, and π^\pm) contribute little to the NaI spectra and are not constrained by our measurements. For simplicity, and given their shared origin in the nuclear component of air showers [30], we scale the hadronic intensity by the same value as the μ^\pm component.

The best-fit scaling for our reference spectrum is 0.79 times the PARMA predictions for the electromagnetic shower components (e^\pm and γ), and 0.88 for the muons and all other species. Measurements made in other rooms on the same site yield scale factors for the PARMA predictions between 0.5 and 0.8 for the electromagnetic components and between 0.85 and 0.88 for the other species.

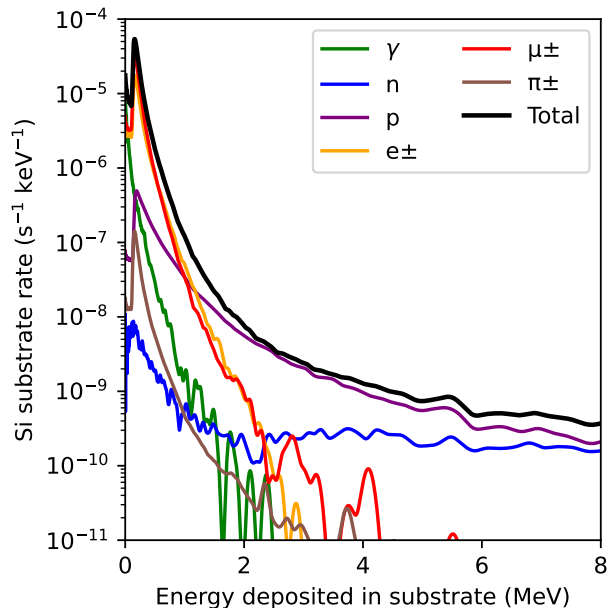


FIG. 5. Energies deposited by cosmic rays (modeled) in a silicon substrate (500 μm thick, 25 mm^2 area), both in total (top curve) and separated by the species of the particle incident upon the circuit. The μ^\pm and e^\pm dominate the interactions by numbers, but nucleons (p and n) cause all of the rare, most energetic events. Charged particles (other than protons) are shown with both charge states combined. The spectra for both charge states of μ and π are very similar, while e^- outnumber e^+ by a 2:1 ratio over most of the spectrum.

We attribute the variation to the range of shielding overburden. Our cosmic-ray model includes the shielding effect of a particular concrete ceiling 18 cm thick. While this model accurately describes conditions of the reference measurement, other spectra were recorded in rooms with additional building levels and more structural materials above them. The NaI measurements show that this additional overburden reduces the e^\pm and γ intensity by as much as 40% but attenuates the highly penetrating μ^\pm component by only a few percent. These effects are consistent with the predictions of GEANT4 models for attenuation in the concrete ceiling of the reference measurement. The rescaling of the PARMA model’s μ intensity by a factor of 0.88 is both small and empirically necessary, as the model is based on interpolations of air-shower simulations. We use the rescaling factors found from NaI measurements to correct the intensities for all cosmic-ray models when we compare them to measurements made in a superconducting circuit.

C. Cosmic rays in a qubit circuit

We model a qubit’s substrate as in Section II: as a 5 mm \times 5 mm square of silicon, diced from a wafer

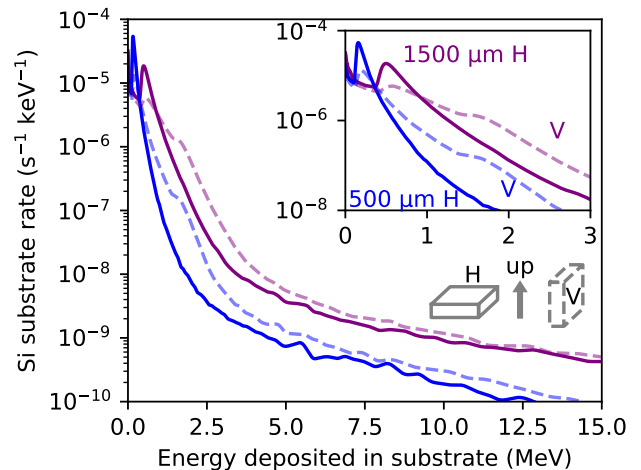


FIG. 6. Simulated energy deposits from cosmic rays (summed over all particle species) in 5 mm \times 5 mm silicon substrates of 1500 μm and 500 μm thickness when oriented horizontally (solid curves) or vertically (dashed). The horizontal 500 μm result is the same as the curve labeled “Total” in Figure 5. The prominent peaks (at 0.52 MeV and 0.17 MeV) in the horizontal model correspond to the typical energy loss of minimum-ionizing μ^\pm and e^\pm passing through silicon along paths approximately equal to the wafer thickness. The cartoon shows our definitions of horizontal (“H”) and vertical (“V”) orientation; the inset highlights the spectra at lower energies.

with one of two thicknesses. Cosmic rays generated by the PARMA model must first pass through intervening materials—the concrete ceiling and aluminum cryostat shells—before entering the silicon substrate. The model predicts the rate of events depositing at least 40 keV to be 0.0075 s^{-1} and 0.0090 s^{-1} for the wafers of 500 μm and 1500 μm thickness, respectively. The corresponding powers are 1.91 keV s^{-1} and 5.3 keV s^{-1} . The uncertainties in these models are dominated by systematic uncertainties that we estimate to be 3%, including the effective volume of the NaI spectrometer used to calibrate the cosmic-ray intensity and the angular distribution and particle-species breakdown of cosmic rays.

The cosmic-ray event rate differs only slightly between the two silicon wafers of very different thickness, while the power deposited scales approximately as the volume. In contrast, for terrestrial gamma rays, both event rate and power scaled approximately with volume. The scaling rules differ because the charged particles that constitute most cosmic rays lose energy almost continuously in multiple scattering events per mm in silicon [31], while a similar amount of silicon is optically thin to photoelectric absorption and Compton scattering at the relevant (MeV-scale) energies. Thus, an energy-loss event is nearly certain for cosmic rays that pass through the silicon wafer but unlikely for any single gamma ray.

Figure 5 shows the distribution of energy deposited by cosmic rays in a silicon substrate, both the overall

spectrum and its breakdown by particle species. The distribution shows that the event rate and total power are dominated by charged leptons, the μ^\pm and e^\pm . On the other hand, the rare events that deposit more than 2 MeV in a 500 μm -thick silicon wafer are almost entirely the result of cosmic-ray protons and neutrons. This result suggests different mitigation strategies, depending on whether the more frequent leptonic events or the more energetic but rarer hadronic events are more disruptive to a given circuit.

One tactic sometimes employed to mitigate cosmic-ray events is to orient the qubit circuit vertically (that is, to align one long dimension of the chip vertically) [13]. Figure 6 shows that this approach changes the spectrum only modestly. Although a vertical orientation does reduce the rate of low-energy events, it increases the rate of higher-energy events. Overall, a vertical orientation reduces the expected rate of cosmic-ray events by approximately one-third, but the mean energy deposited per event grows by a similar factor, so that the power deposited is reduced by only 2% for our specific geometry. Because gamma rays emitted isotropically from a large, unshielded floor are likely to be even less affected by circuit orientation, this particular design choice would appear to offer limited benefits.

Cosmic rays produce events at a wide range of energies, but at energies below ~ 1.5 MeV, they contribute less to the predicted spectrum than the gamma rays emitted by terrestrial sources under the conditions found in our laboratories. Cosmic-ray secondaries are still important, however, because their energies can be much higher than the ~ 2.6 MeV maximum of the gamma-ray events. Nucleons (protons and neutrons) in the cosmic rays are thus responsible for the upper region of the absorbed-energy spectrum (Figure 5 for the 500 μm -thick silicon, or Supplemental Material Figure A.2 for the 1500 μm substrate). Section VII discusses the relative importance of cosmic rays and terrestrial gammas for devices on silicon wafers, which depends both on the substrate thickness and the circuit's sensitivity to the lower-energy events.

IV. THERMAL KINETIC INDUCTANCE DETECTORS AS A PROBE OF BACKGROUNDS

The results shown so far consist of measured and simulated backgrounds in a large scintillator detector, and simulated backgrounds in a superconducting circuit. The scintillator measurements allow us to calibrate the intensities of the simulated backgrounds. We have also made measurements with a type of calorimetric detector very similar to a typical superconducting qubit in most respects. In this section, we describe that detector. It is uniquely suited to the goal of validating the background models, as it enables spectroscopic study of the energy deposited in a volume of silicon similar to the substrate of a quantum circuit, over a suitable range of energies.

The microcalorimeters used in this study are based on

the microwave kinetic inductance detector (MKID) [7, 32]. The MKID is a cryogenic detector technology that exploits the exceptionally high kinetic inductance of a superconductor to measure the energy of incident radiation events. In an MKID, a thin superconducting film is fabricated into a microresonator circuit. When energy is deposited in the superconducting resonator, Cooper pairs are broken. With fewer pairs to carry the supercurrent, the kinetic inductance grows, decreasing the resonant frequency. The magnitude of the frequency shift depends on the energy absorbed in the radiation interaction event, enabling spectroscopic measurements.

A thermal kinetic inductance detector (TKID) calorimeter [33–35] incorporates a structure to absorb and thermalize energy. The absorber can be co-located with the superconducting resonator and isolated on a micromachined island to confine thermal energy long enough for accurate measurement. In this work, the micromachined island is itself the radiation absorber and there is no separate absorbing structure. The TKID is similar in many ways to the more mature transition-edge sensor (TES) calorimeter [36–38], but its silicon absorber and well-defined interaction volume made it especially suited for this work.

Being a less mature detector technology, however, TKIDs are not without their disadvantages. In particular, the device physics is less thoroughly understood, and the energy resolution of current devices for photon detection is significantly worse than that achieved in the best TESs. For the current measurement, the broad dynamic range is far more important than the energy resolution.

We have fabricated a pair of TKID calorimeters to probe radiation backgrounds [39], the main difference between the two devices being the thickness of the silicon substrate (500 μm and 1500 μm). The fabrication began with the deposition of the superconducting titanium nitride (TiN) layer. The stoichiometry, and therefore superconducting critical temperature, T_C , of the film was controlled through the proximity effect [40, 41] by depositing alternating layers of Ti and TiN [42]. The 14 TiN films each have nominal thickness 5 nm, and the 13 intervening Ti films are each 10 nm thick, giving the overall thin film a nominal thickness of 200 nm. The T_C of this composite superconducting film was measured to be 850 mK. The film was lithographically patterned and etched to form the resonator and microstrip transmission line structures. Additionally, gold films were deposited on the outer regions of the chip to support thermalization to its copper enclosure through gold wire bonds. Finally, a deep reactive ion etch (DRIE) was used to define and isolate the radiation-absorbing island. The island is 5 mm square for both devices. The deep etch goes entirely through the wafer, and the TKID island thickness is simply equal to the original substrate thickness. This island area was chosen to be representative of a typical quantum circuit. The thinner wafer is in the range commonly used for superconducting circuits, while the thicker one was chosen to help us validate models of scaling with

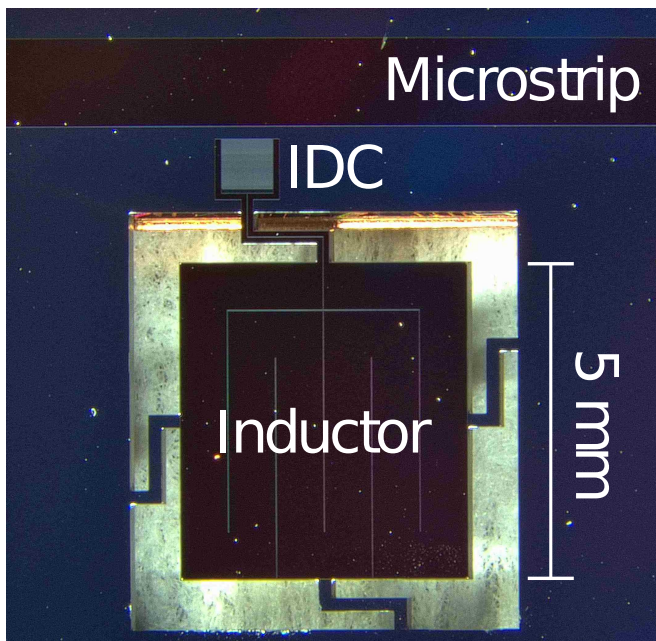


FIG. 7. Micrograph of the 500 μm thick TKID. The TiN-Ti resonator structure consists of a meandered inductor on the island and an interdigitated capacitor (IDC) on the bulk substrate. The IDC is capacitively coupled to the microstrip transmission line running horizontally across the top of the image. The 5 mm \times 5 mm island is thermally coupled to the substrate only through its four legs. The legs are approximately 200 μm wide and 1500 μm long. Gold films and gold wire bonds on the outer regions of the chip (not pictured) are used to thermalize the substrate.

thickness. Figure 7 depicts the 500 μm thick device. The devices were operated at a temperature of 175 mK, well below the superconducting film’s critical temperature.

V. TKID MEASUREMENTS OF RADIATION BACKGROUNDS

The readout of TKIDs and the data analysis procedures are described in detail in the Supplementary Material, Section A 2. In short, a microwave probe tone at the resonant frequency is sent through the cryostat, coupled to the resonator, amplified, and mixed against a reference tone to determine the amplitude and phase of the transmitted tone. Changes in the complex transmission indicate a shift in the resonant frequency due, in this case, to temperature changes in the TKID island. These values are digitally sampled once every 800 ns. The TKID response to a radiation event is a transient pulse.

One important requirement for this measurement is sensitivity over a wide range of energies with reasonably good linearity. Changes in the TKID resonant frequency are nearly proportional to changes in the TKID temperature for a wide range of energies deposited in the device, up to several MeV. Deposition of energy E heats

the TKID island, increasing the temperature T by $\delta T = E/C(T)$, where C is the (weakly temperature-dependent) heat capacity. The equilibrium population of quasiparticles (broken Cooper pairs) in the superconducting film depends on temperature as $n_{\text{QP}} \propto \sqrt{T} \exp(-\Delta/kT)$ [32], where Δ is the superconducting gap energy. The gap Δ equals $1.76kT_C$ in BCS theory [43]. Although quasiparticle population changes are not linear for large changes in temperature, we have designed the TKID such that even the most energetic events increase T by no more than 1%. Changes in quasiparticle density, in turn, cause proportional changes in the thin-film resonator’s inductance, and proportional shifts in the resonant frequency. Though this chain of relationships contains multiple departures from strict proportionality, most are small for MeV-scale events in our TKIDs. Furthermore, the positive curvature of the function $n_{\text{QP}}(T)$ and the fact that silicon’s cryogenic heat capacity grows with temperature act as nonlinearities of opposite sign. We estimate that the nonlinear effects due to heat capacity and quasiparticle population change our energy estimates by no more than 20% at 10 MeV (the highest energy detected in the background spectrum). Below 1 MeV, they are less than 3% and subdominant to the overall energy-scale calibration uncertainty.

The radiation backgrounds were measured for 168.0 hours with the 500 μm TKID and for 97.5 hours with the thicker 1500 μm device, both in the horizontal orientation (as defined in Figure 6). These data were collected with hourly gaps of approximately 100 seconds in which the resonator transmission was re-characterized in case of drifts. In addition to the background data, 5.0 and 3.0 hours were devoted to measurements of a sealed ^{153}Gd radiation check source. This source produces emissions of known energies, which we use for energy calibration.

The TKID pulses are found to fall with two distinct exponential time constants, typically around 60 μs and at least 240 μs . The slower time constant corresponds to the ratio of the island’s heat capacity to the thermal conductance of the TKID island’s four legs. To optimize the energy resolution and linearity, we estimate only the amplitude of the slower, thermal component from each pulse and discard information about the (small) amplitude of the other component.

The TKID shown in Figure 7 is sensitive primarily to energy deposited in the square island, but it is not fully immune to the passage of particles that deposit energy in the surrounding frame. Tests with a pulsed diode laser (wavelength 635 nm) aimed first at the island and then at the frame show that optical energy absorbed in the frame can produce a TKID signal with amplitude a few percent of the signal produced by equivalent optical events aimed at the center of the island. The largest of these “frame events” can be identified and removed from the data because of their unusually slow signal rise and fall times, but the smaller examples cannot be reliably identified. As a result, the measured flux at inferred energies of less than approximately 200 keV is subject to systematic un-

certainties and almost certainly overestimates the true flux incident on the TKID island.

The most intense emission from the ^{153}Gd calibration source is a pair of gamma rays at 97 keV and 103 keV, but silicon wafers as thin as our TKIDs have negligible photo-absorption at these energies. Instead, the characteristic $K\alpha$ and $K\beta$ emission of the europium decay product was used for calibration. These x-ray lines (41 keV and 47 keV) [44] are unresolved by the TKID and produce a weighted-average energy of 42.2 keV. To confirm that the calibration line was indeed x-ray emission of the excited Eu and not the 100 keV gamma rays, we verified that the observed line intensity was reduced by the expected factor of 2.2 when a copper foil 203 μm thick was placed in between the check source and the sensor, rather than the factor of 1.1 that would be expected if the observed peak were actually 100 keV [45].

The 42 keV calibration peak also establishes an approximate energy resolution of 10 keV (full-width at half-maximum) in the thicker TKID and 20 keV in the thinner device. This resolution is far from the intrinsic thermal-fluctuation limit of the TKID calorimeters. Possible reasons for the poor resolution include a position-dependent response, non-optimal microwave readout tone power or frequency, and gain drift. It is uncertain whether the resolution is a constant amount of energy, or a fixed fraction of the measured energy, or something in between.

Gain stability is difficult to assess from such a spectrum. The ^{153}Gd check source shows the 42 keV peak changing by no more than $\pm 10\%$ from one 30-minute measurement to the next. The pulsed laser coupled to the TKID via an optical fiber shows evidence of gain variations at least this size over ten-minute timescales. Gain drifts do not seem to limit the energy resolution of the current device, yet are large enough to require improvement in future systems. It is not clear whether the drifts are due to changes in the cryostat temperature, in the magnetic environment, or merely in the optical system used to assess the gain variations.

The same laser was used with a variable optical attenuator to check the linearity of the TKID sensor. The sensor response is consistent with linearity. The data show a response that grows as the $\alpha = 1.03 \pm 0.05$ power of the optical pulse energy, up to pulses approximately 100 times the amplitude of the 42 keV events from the check source. This verifies the energy response up to 4 MeV and shows it to be both close enough to linear for the assessment of radiation backgrounds, and consistent with our theoretical understanding of nonlinear effects below 10 MeV. The main systematic uncertainty on this linearity test is the limited stability of the TKID-plus-laser as a consistent energy standard.

The limitations on TKIDs' energy resolution and linearity and on our ability to perform energy calibrations will be addressed in future sensor designs and future readout optimizations. The TKID is a fairly new technology among superconducting microcalorimeters, and problems are to be expected. Nevertheless, it is already a valuable

E_{\min} (keV)	Component	Event Rate (s^{-1})	Power (keV s^{-1})	Mean E (keV)
0	Gamma rays	0.0255	3.14	123
0	Cosmic rays	0.0080	1.92	241
0	Model total	0.0332	5.06	153
40	Gamma rays	0.0153(7)	2.98(15)	194
40	Cosmic rays	0.0075(2)	1.91(6)	255
40	Model total	0.0227(7)	4.89(15)	215
40	Model + frame	0.035(4)	5.9(4)	n/a
40	TKID measured	0.0331(2)	6.3(3)	190

TABLE II. Model and measurement of the rate of energy-absorption events, the power they deposit, and the mean energy per event for the 500 μm -thick silicon substrate. The substrate is square with area 25 mm^2 . All values represent integrals from E_{\min} to 20 MeV. The first three lines represent the full integral (that is, from a minimum energy of 0), relevant for instruments with high sensitivity to even the smallest background events. The next three lines represent the models integrated starting at 40 keV, where the current measurements are most reliable. These lines give the results of the gamma-ray model (Section II), the cosmic-ray model (Section III), and their sum. The Model + frame line also adds a model of the excess events that are detected in the TKID island even though the energy was deposited in the frame; this line is most appropriate for comparison to the measured rates. The estimated uncertainties in parentheses are all dominated by various systematic uncertainties, except for the measured TKID event rate, which is dominated by Poisson statistical uncertainty. The frame-hit model has 30% relative uncertainties. Equivalent results for the thicker silicon substrate appear in the Supplemental Material Table A.1.

tool for measuring energy deposited in a superconducting circuit by charged-particle and gamma-ray backgrounds.

VI. COMPARISON OF MODEL AND MEASUREMENT

Figures 8 and 9 show the radiation background spectrum measured by both TKIDs, compared to our background models. This comparison is not a fit to the TKID data—the models are adjusted based only upon the NaI measurements. According to the models, lowest-energy events are primarily due to terrestrial gamma rays, while events depositing 2 MeV or more are mostly the result of cosmic rays (primarily protons and neutrons, as Figure 5 shows). At intermediate energies, both sources of backgrounds are of comparable intensity. A peak in the cosmic-ray component of the model appears near 520 keV in the 1500 μm sensor and near 170 keV in the 500 μm sensor (Figure 9). This peak is the product of an abundance of minimum-ionizing particles (e and μ) traversing similar path lengths through the silicon, paths approximately equal to the substrate thickness. Because the gamma-ray spectrum equals or exceeds the cosmic-ray spectrum at these energies, the predicted cosmic-ray peak

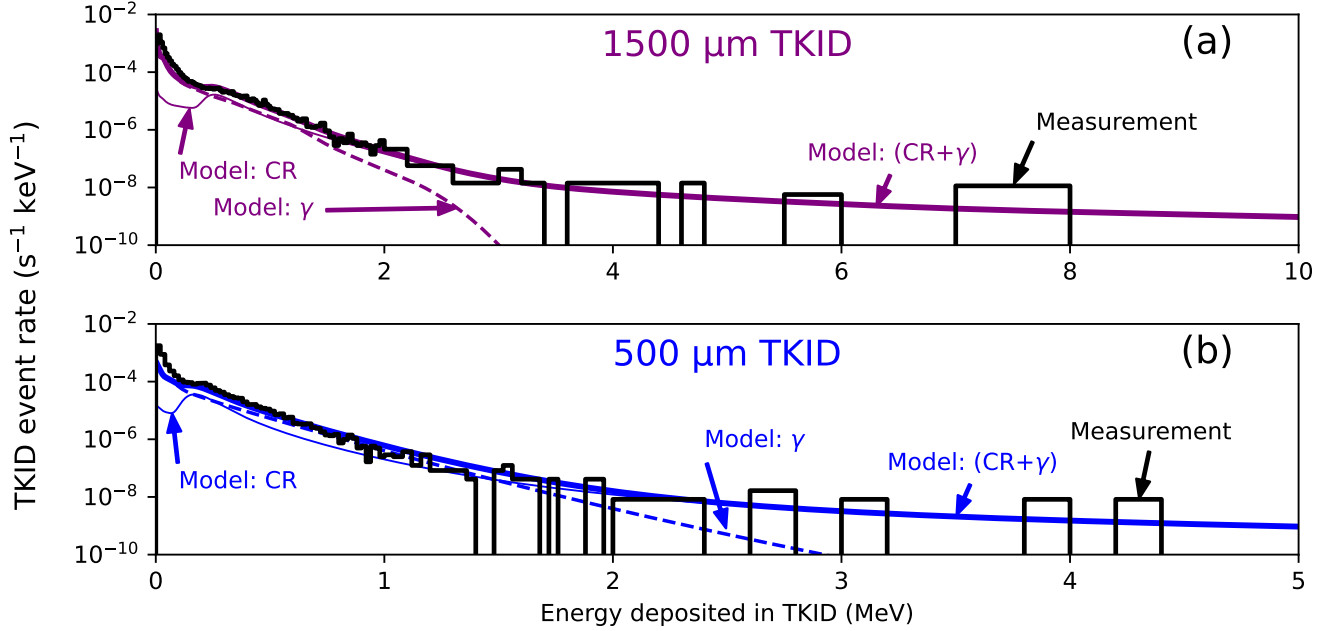


FIG. 8. Measured background spectrum from TKIDs made of silicon 1500 μm thick (a) and 500 μm thick (b), both in the horizontal orientation (as defined in Figure 6). Also shown in each panel are the model predictions for terrestrial gamma rays (“Model: γ ”, dashed) and cosmic rays (“Model: CR”, thin solid line), and their sum (thicker solid line). The measured spectrum uses unequal bins to reduce visual distraction where events are rare: 50 bins per MeV below 1 MeV; 20 per MeV up to 2 MeV; 5 per MeV up to 5 MeV; and 2 per MeV above 5 MeV. The measurements and models agree well, within a factor of 1.5 through most of the energy range studied. The discrepancy at the lowest energies arises because the measurement includes frame events, while the model curves exclude any frame events (see text). Figure 9 shows the low-energy region in more detail.

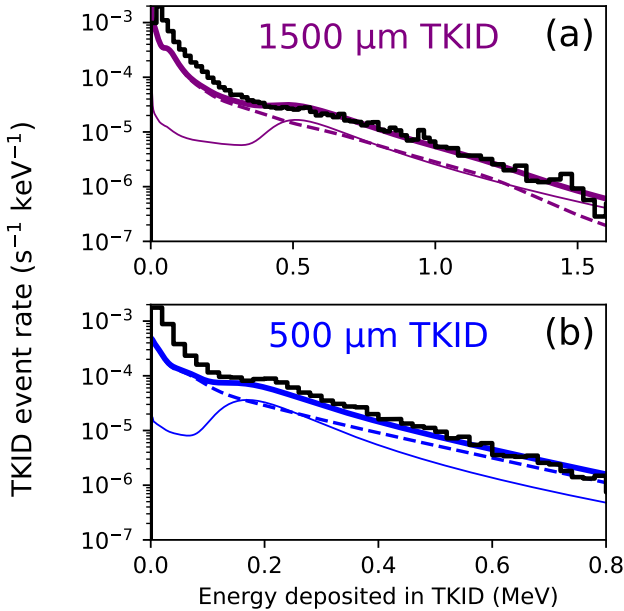


FIG. 9. Measured background spectrum from TKIDs made of silicon 1500 μm thick (a) and 500 μm thick (b) compared to models of the spectra. The plotted curves are the same as in Figure 8 but show only the lower-energy events.

is largely obscured. It appears in the measurements (and the composite model) as a subtle feature rather than a clear hump.

No matter how linear the TKID may be in response to energy, the measurement has a systematic uncertainty of at least $\pm 5\%$ on the energy scale. The limited number of events at the calibration line of 42 keV and the lack of calibration features above that energy are the primary reasons for this uncertainty. This systematic alone is adequate to bring the data and model into excellent consistency across most of the wide energy range measured here, though we have *not* used this freedom to adjust the measurements depicted in Figures 8 and 9.

For measured energies below approximately 200 keV, an additional source of uncertainty and bias in the event rate is present: particles that deposit energy in the silicon frame can produce an unwanted thermal signal in the TKID island. As discussed in Section V, we attempted to eliminate such frame events from the spectrum based on their distinctive pulse shape, but reliable discrimination is difficult. Frame hits cause small pulses with low signal-to-noise ratios. The result is a limited effectiveness of this test for events with apparent energy less than ~ 200 keV, which produces a bias towards overestimation of the spectrum at lower energies. In the Supplemental Material (Appendix A), we discuss a model of frame hits that explains the measured excess. However, the model

curves shown in Figures 8 and 9 do not include an estimated frame-hit contribution.

Across the range of energies from 200 keV to 10 MeV, the measurement of the spectrum agrees well with the model of the background radiation, almost everywhere to within a factor of 1.5 in the count rate. We stress that no free parameters were fit to match the models to the measurement—all re-scalings in the intensities of the models were determined from the entirely independent NaI measurements. Figures 8 and 9 present absolute-rate comparisons of model and measurement. This means that our radiation models, their intensities normalized to measurements taken by a NaI spectrometer with a volume of $347\,000\text{ mm}^3$, also describe the spectrum of energy deposited into silicon structures with volumes as small as 12.5 mm^3 inside a millikelvin refrigerator. Therefore, the models represent valid tools to predict the impact of background radiation on millimeter-scale silicon devices such as superconducting quantum circuits.

Table II summarizes the comparison between model and measurement for the $500\text{ }\mu\text{m}$ TKID, integrated over energy. (The analogous result for the thicker TKID is in the Supplemental Material, Table A.1). The base model shows a lower rate of events and of power deposited in the island compared to the measurement. When the model is enhanced by the expected consequences of frame hits, however, the measurements agree well. The predicted event rate is 7% higher than the measurement, while the power is 7% lower. We consider this to be very good agreement given the simplified models, and also given that the spectrum was integrated well down into the range where frame events and island events cannot readily be discriminated. The rates quoted in the table apply to an island with thickness $500\text{ }\mu\text{m}$ and area of 25 mm^2 , but to a good approximation, the values for other sizes at fixed thickness should be proportional to the island area. Section VII and Figure 10 explore the scaling to thinner substrates.

VII. REDUCING THE IMPACT OF BACKGROUND RADIATION ON QUANTUM CIRCUITS

Our results shed light on the effectiveness of various strategies for mitigating the effects of background radiation on superconducting circuits, such as TKIDs and qubits. We argued in Section III C that a chip’s orientation (vertical or horizontal) has limited effects. Still, mitigation strategies are possible: use of smaller substrate volumes, shielding, and thermal isolation of critical areas.

The curves of Figure 8 show that at any given energy above 0.5 MeV, the rate of background events is roughly a factor of 5–10 higher in the $1500\text{ }\mu\text{m}$ thick device compared to the $500\text{ }\mu\text{m}$ device. After integrating the predictions of our background model over energy, we find that the total event rate (power) is 2.3 (2.8) times higher in the $1500\text{ }\mu\text{m}$ device than in the $500\text{ }\mu\text{m}$ device. Clearly,

superconducting circuits on smaller substrates will experience less disruption from background radiation. A substrate can be made smaller by reducing either its area or its thickness.

It is useful to consider the spectra of background events in substrates spanning a wider range of thickness than the two values probed experimentally in this work. The typical thickness of a 300 mm-diameter silicon wafer is $775\text{ }\mu\text{m}$, so substrates thicker than our $1500\text{ }\mu\text{m}$ sensor are unlikely. However, substrates thinner than $500\text{ }\mu\text{m}$ are both realistic and interesting as a means of reducing the radiation background. Silicon becomes difficult to handle at thicknesses below $100\text{ }\mu\text{m}$, but the device layer in silicon-on-insulator (SOI) wafers can be thinner than $1\text{ }\mu\text{m}$. Standard micro-machining techniques can be used to remove the handle layer from underneath selected circuit regions on SOI substrates. Such techniques offer a path to substrates with thickness of a few μm or less. Consequently, in Figure 10 we show models estimating the event rate and dose rate for substrates with thicknesses from $1\text{ }\mu\text{m}$ to $1500\text{ }\mu\text{m}$.

Cosmic-ray event rates and power deposition in $500\text{ }\mu\text{m}$ wafers are dominated by charged particles (primarily μ^\pm and e^\pm), as shown in Figure 5. Models over the wider range of wafer thickness (Figure 10) display the expected behavior: cosmic-ray power grows in proportion to the wafer thickness, while the event rate stays approximately constant. The event rate does grow slightly with the thickness, as an increasing lateral area of the silicon island is exposed to cosmic rays arriving from non-vertical directions.

The effects of terrestrial gamma rays depend differently on the wafer thickness. For thicker wafers, the event rate is proportional to thickness, as expected given the low probability of gamma-ray scattering. The rate approaches a non-zero value for thin substrates, however, due to incident gamma rays that eject secondary electrons from nearby packaging. This minimum suggests that a final shield around the qubit could be beneficial, particularly for thinner wafers. Relative to a higher- Z metal of equal mass, a shield made of a low- Z material (such as graphite) would block electrons more effectively [46] while interacting less with gamma rays, suppressing the rate of events due indirectly to terrestrial gamma rays [31].

The power deposited by terrestrial gamma rays grows faster than the thickness, because the primary mechanism for interaction of MeV-scale gamma rays with silicon is Compton scattering. Scattered electrons are not only more numerous in thicker wafers, but they also travel longer paths and are able to deposit a larger fraction of their energy. Overall, the use of thinner substrates reduces the power deposited by background radiation in proportion to the thickness reduction, but the event rate falls no lower than approximately $4 \times 10^{-4}\text{ s}^{-1}\text{ mm}^{-2}$, even for very thin substrates.

An interesting result shown in Figure 10 is that muons cause the majority of the disruptive cosmic-ray events

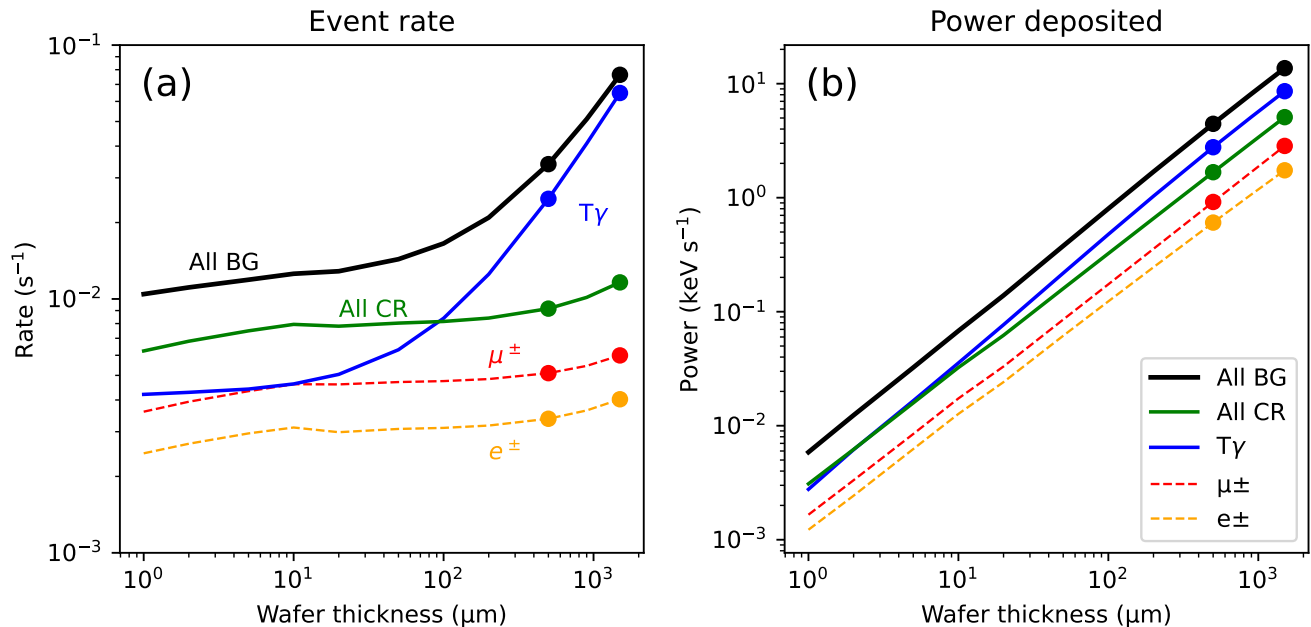


FIG. 10. Dependence of event rates (a) and background power (b) on silicon wafer thickness, integrated from 40 keV to 20 MeV as in Table II. Rates and power are modeled for a $5 \times 5 \text{ mm}^2$ device inside a simplified model of a cryostat; both should scale approximately as the device area. The values come from the models validated by our TKID measurements but extended to thinner substrates. Thicknesses modeled include 1 μm , 2 μm , 5 μm , 10 μm , 20 μm , 50 μm , 100 μm , 200 μm , 500 μm , 900 μm and 1500 μm . The two thicknesses corresponding to our TKID measurements are indicated by circular markers. Dashed lines are the μ^\pm and e^\pm components of cosmic rays. Because interactions due to the p , n , γ , and π^\pm components are far less common, with rates well below $3 \times 10^{-4} \text{ s}^{-1}$, they are not shown separately. The sum of all cosmic-ray components is green. The events caused by terrestrial gamma-ray emission (“T γ ”) are shown in blue. The sum of all backgrounds is black. While the power scales with substrate thickness, cosmic rays impose a minimum event rate for even the thinnest substrates.

and power, yet electrons’ contributions are only a factor of two smaller. This fact suggests that shielding an instrument from most e^\pm secondaries could reduce cosmic-ray events and power by as much as $\sim 1/3$, without requiring a muon-blocking, deep underground site.

The structure of our TKID devices shows that micromachining can produce silicon islands connected to a surrounding frame of silicon only by narrow beams or legs. Circuitry placed on such an island is partially thermally isolated from background events that occur in the frame, suggesting the use of micromachined moats to isolate critical areas of a superconducting quantum circuit from the larger surrounding chip. Measurements illuminating the frame area with laser light at a specific spot 1 cm from our TKID showed a thermal response in the TKID approximately 3% of the response from direct illumination of the island, thus demonstrating the viability of such protection schemes. The effectiveness of a moat will depend heavily on the details of its implementation; superior protection should be achievable with thinner legs than used here, along with additional heat sinking of the silicon frame.

Sapphire substrates are also used for superconducting qubits [47]. Cosmic rays and gamma rays transfer energy to sapphire by the same mechanisms we have modeled for

silicon, yielding quantitatively similar spectra for equal column densities. The cross sections for Compton scattering of photons and the Bethe-Bloch mean energy-loss formulas for charged particles are nearly equal for sapphire and silicon [31]. Given the densities of 4.0 g cm^{-2} for sapphire and 2.3 g cm^{-2} for silicon, losses and event rates in a 300 μm sapphire wafer and in a 500 μm silicon wafer should be nearly the same. In a full GEANT4 model of cosmic rays, we find the spectrum of events is nearly identical above 100 keV in the two wafers. The thicker silicon wafer shows more events at lower energies, in a ratio of 5/3, as expected given their different lateral areas (Supplemental Material Figure A.5). GEANT4 models of the terrestrial gamma-ray spectrum also show equivalence between the two substrates with equal column density.

In an unshielded laboratory setting, and for any realistic substrate thickness, gamma rays deposit more power than cosmic rays and cause more—or at least a comparable number of—events (Figure 10). To shield superconducting quantum circuits from gamma rays is therefore worthwhile. Attenuation of gamma rays by a factor of e at 1 MeV requires only 21 mm of steel or 12 mm of lead [45], though one must account for muon-induced secondaries produced in such a shield. In the complete

absence of gamma rays, the power we observed would be reduced by a factor of three for the thicker wafers, and the event rate by a factor of at least five. The relative benefits would be smaller but still important for wafers thinner than 100 μm .

If gamma rays could be fully screened, the remaining cosmic contribution would be dominated by μ^\pm and e^\pm . While electrons are not difficult to stop, muons are highly penetrating and can only be attenuated by operating underground. Still, the most energetic and therefore the most disruptive events are caused by protons and neutrons. Robust superconducting quantum circuits are likely to benefit from a range of shielding strategies, some intended to suppress the most common events and others targeted at the most energetic events.

VIII. CONCLUSIONS

We have modeled two sources of naturally occurring background radiation that are dominant in an unshielded surface laboratory: cosmic rays and radiogenic gamma rays from terrestrial sources. We used a commercial NaI detector to measure the intensities of the key components of these models. We then checked the validity of these same models for silicon substrates with sizes typical of those used in superconducting qubits. Specifically, we performed spectroscopic measurements of the backgrounds inside a millikelvin cryostat with two TKID devices, superconducting energy-resolving detectors of photons and charged particles. The measurements provide both event rates and incident power levels for silicon substrates that are 500 μm and 1500 μm thick (Tables II and A.1, respectively). No additional free parameters were required to match model and measurement to within $\pm 7\%$. For the 500 (1500) μm thick device, the modeled average event energy is 215 (293) keV. (The measured average event energies are skewed towards lower values by the numerous low energy frame events.) However, the background events have a broad spectrum whose high energy tail extends well into the MeV range. Circuit features designed to mitigate the effects of the average background event may be insufficient for events in this high energy tail. The modeled and measured radiation spectra are highly compatible over an energy range that spans a factor of about 25 and an energy-dependent event rate (in units of $\text{s}^{-1} \text{keV}^{-1}$) range that spans a factor of about 10^6 . This success shows that established tools for modeling particle and radiation transport can be used productively to describe the radiation backgrounds in superconducting device substrates, although care is needed in the construction and application of a background model.

Our measurements were made in one specific above-ground laboratory, at moderately high elevation. Still, with appropriate correction factors, the results should apply to any other above-ground facility. Given our location and substrate sizes, we found the effects of gamma rays to be larger than those of cosmic rays, but not over-

whelmingly so. The highest energy, MeV-scale events, are entirely the result of cosmic rays, specifically protons and neutrons. Cosmic-ray secondaries would be reduced (by approximately 25%) at sea level, or further for instruments placed only a few meters underground. The effects of gamma radiation can be reduced by the use of low-activity building materials, or by shielding with a few centimeters of steel or lead.

While these measures are feasible, the difficulty of shielding both terrestrial gamma rays and cosmic rays also argues for the development of superconducting circuit designs that are intrinsically robust to background radiation. We have shown here that the effects of background radiation can be reduced by shrinking the circuit substrate in area or thickness, or by using micro-machining to thermally isolate critical substrate regions from the larger chip. Other mitigation measures not explored here are also possible such as: the use of thin films to absorb and thermalize phonons created by background events; superconductor gap-engineering to reduce the quasi-particle density in sensitive circuit regions; or on-chip sensors to detect and veto background events.

Because the TKIDs demonstrated here are compatible with both the fabrication of superconducting qubits and the techniques used to read them out, it should be possible to include TKIDs or closely related MKIDs in quantum circuits. In dispersive qubit readout, the state of the qubit is encoded in the characteristic frequency of another structure, typically a microresonator, that is coupled to a microwave transmission line [48]. In both MKIDs and qubits, the resonant frequency is probed with a microwave tone. In fact, MKIDs and qubits with different frequencies could share a common transmission line. In the future, MKIDs that are co-fabricated with a quantum processor or that are located nearby can act as explicit and unambiguous detectors of background events, offering potential advantages for extremely local active vetoes of background events [49].

We find several lessons in the modeling we have performed and in the measurements we have made with both conventional spectrometers and the TKID superconducting sensors. We find the PARMA model of atmospheric secondary cosmic rays to be good, though the best match to our measurements required rescaling the hadronic component (including muons) by 0.88 and the electromagnetic component by a location-varying factor ranging between 0.5 and 0.8. Apart from the intensity scaling, we argue it is essential to include species other than muons in the cosmic ray model: electrons and gamma rays make significant contributions to the backgrounds in silicon at the same energies as muons do, while protons and neutrons generate rare events at substantially higher energies. For terrestrial gamma rays, the spectra acquired in three widely separated sites varied greatly in intensity (by a factor of 4), but not in shape. An assumption of secular equilibrium in the ^{238}U and ^{232}Th decay chains is supported by the measured spectra, considerably simplifying construction of the back-

ground models. The data support a break in equilibrium at the radon step in the ^{232}Th chain with a 3/2 activity ratio; the data do not constrain the pre-radon section of the ^{238}U chain. To model the spectrum correctly, it is necessary to account for Compton scattering of the terrestrial gamma-ray background. Finally, for the conditions studied here (an unshielded, ground-level laboratory, with devices on silicon substrates and most reliable for events with $E > 40\text{ keV}$), shielding by the cryostat body and the laboratory ceiling plays only a modest role. As a result, highly simplified geometric models of these components were adequate.

In summary, we present the first spectroscopic measurement of background events in a silicon die whose size and temperature is representative of the substrates used in superconducting quantum circuits. A model of these radiation backgrounds as the result of naturally occurring radioisotopes and of cosmic rays has been matched to our specific local conditions by measurements performed with a standard, commercially available gamma-ray spectrometer. This model, without any additional free parameters, agrees quantitatively with spectral measurements of the radiation background performed with energy sensors similar in size and composition to many quantum circuits. We use the models to demonstrate how different components of the background respond to changes in the substrate thickness. We anticipate that this model-

ing approach and the measurement result will be broadly useful to the QIS and superconducting sensor communities.

Data and code availability: The Microcalorimeter Analysis Software System (MASS) repository used for the analysis of the TKID data in this work is available at https://bitbucket.org/joe_fowler/mass. The data and all other code used in this study are available from the corresponding author upon reasonable request.

Official contribution of the National Institute of Standards and Technology; not subject to copyright in the United States.

ACKNOWLEDGMENTS

We thank Adam Sirois and Dan Becker for helpful suggestions on this manuscript. We gratefully acknowledge support from the U.S. Department of Energy (DOE). This work was supported by the DOE Office of Science, Office of Nuclear Physics, under Award Numbers DE-SC0021415 and DE-SC0023682. Pacific Northwest National Laboratory is a multi-program national laboratory operated for the U.S. DOE by Battelle Memorial Institute under Contract No. DE-AC05-76RL01830.

-
- [1] S. Bravyi, O. Dial, J. M. Gambetta, D. Gil, and Z. Nazario, The future of quantum computing with superconducting qubits, *Journal of Applied Physics* **132**, 160902 (2022).
- [2] M. Kjaergaard, M. E. Schwartz, J. Braumüller, P. Krantz, J. I.-J. Wang, S. Gustavsson, and W. D. Oliver, Superconducting qubits: current state of play, *Annual Review of Condensed Matter Physics* **11**, 369 (2020).
- [3] G. Burkard, T. D. Ladd, A. Pan, J. M. Nichol, and J. R. Petta, Semiconductor spin qubits, *Rev. Mod. Phys.* **95**, 025003 (2023).
- [4] A. P. Vepsäläinen, A. H. Karamlou, J. L. Orrell, A. S. Dogra, B. Loer, F. Vasconcelos, D. K. Kim, A. J. Melville, B. M. Niedzielski, J. L. Yoder, S. Gustavsson, J. A. Formaggio, B. A. VanDevender, and W. D. Oliver, Impact of ionizing radiation on superconducting qubit coherence, *Nature* **584**, 551 (2020).
- [5] M. McEwen *et al.*, Resolving catastrophic error bursts from cosmic rays in large arrays of superconducting qubits, *Nature Physics* **18**, 107 (2022).
- [6] J. M. Martinis, Saving superconducting quantum processors from decay and correlated errors generated by gamma and cosmic rays, *npj Quantum Information* **7**, 90 (2021).
- [7] J. Zmuidzinas, Superconducting microresonators: Physics and applications, *Annual Review of Condensed Matter Physics* **3**, 169 (2012).
- [8] L. Cardani *et al.*, Reducing the impact of radioactivity on quantum circuits in a deep-underground facility, *Nature Communications* **12**, 2733 (2021).
- [9] C. D. Wilen, S. Abdullah, N. A. Kurinsky, C. Stanford, L. Cardani, G. D’Imperio, C. Tomei, L. Faoro, L. B. Ioffe, C. H. Liu, A. Opremcak, B. G. Christensen, J. L. DuBois, and R. McDermott, Correlated charge noise and relaxation errors in superconducting qubits, *Nature* **594**, 369 (2021).
- [10] K. Karatsu, A. Endo, J. Bueno, P. J. de Visser, R. Barends, D. J. Thoen, V. Murugesan, N. Tomita, and J. J. A. Baselmans, Mitigation of cosmic ray effect on microwave kinetic inductance detector arrays, *Applied Physics Letters* **114**, 032601 (2019).
- [11] V. Iaiia, J. Ku, A. Ballard, C. P. Larson, E. Yelton, C. H. Liu, S. Patel, R. McDermott, and B. L. T. Plourde, Phonon downconversion to suppress correlated errors in superconducting qubits, *Nature Communications* **13**, 6425 (2022).
- [12] P. Du, D. Egana-Ugrinovic, R. Essig, and M. Sholapurkar, Sources of low-energy events in low-threshold dark-matter and neutrino detectors, *Phys. Rev. X* **12**, 011009 (2022).
- [13] B. Loer, P. M. Harrington, B. Archambault, E. Fuller, B. Pierson, I. Arnquist, K. Harouaka, T. D. Schlieder, D. K. Kim, A. J. Melville, B. M. Niedzielski, J. K. Yoder, K. Serniak, W. D. Oliver, J. L. Orrell, R. Bunker, B. A. VanDevender, and M. Warner, Abatement of ionizing radiation for superconducting quantum devices (2024), [arXiv:2403.01032](https://arxiv.org/abs/2403.01032) [quant-ph].
- [14] C. Papastefanou, S. Stoulos, and M. Manolopoulou, The radioactivity of building materials, *Journal of Radioana-*

- lytical and Nuclear Chemistry **266**, 367 (2005).
- [15] S. Nemlioglu, N. Sezgin, and B. O. Cumali, Natural radioactivity in cement, in *Advances in the Toxicity of Construction and Building Materials* (Woodhead, 2022) Chap. 8, pp. 171–206.
- [16] S. Chu, L. Ekström, and R. Firestone, *WWW Table of Radioactive Isotopes*, database version 1999-02-28.
- [17] S. Agostinelli *et al.*, Geant4—a simulation toolkit, *Nuclear Instruments and Methods in Physics Research Section A: Accelerators, Spectrometers, Detectors and Associated Equipment* **506**, 250 (2003).
- [18] J. Allison *et al.*, Geant4 developments and applications, *IEEE Transactions on Nuclear Science* **53**, 270 (2006).
- [19] J. Allison *et al.*, Recent developments in Geant4, *Nuclear Instruments and Methods in Physics Research Section A: Accelerators, Spectrometers, Detectors and Associated Equipment* **835**, 186 (2016).
- [20] J. Perl, J. Shin, J. Schümann, B. Faddegon, and H. Paganetti, TOPAS: An innovative proton Monte Carlo platform for research and clinical applications, *Medical Physics* **39**, 6818 (2012).
- [21] B. Faddegon, J. Ramos-Méndez, J. Schuemann, A. McNamara, J. Shin, J. Perl, and H. Paganetti, The TOPAS tool for particle simulation, a Monte Carlo simulation tool for physics, biology and clinical research, *Physica Medica* **72**, 114 (2020).
- [22] A. Suzuki, T. Iida, J. Moriizumi, and Y. Sakuma, The effects of different types of concrete on population doses, *Radiation Protection Dosimetry* **90**, 437 (2000).
- [23] K.-H. Kampert and A. A. Watson, Extensive air showers and ultra high-energy cosmic rays: a historical review, *The European Physical Journal H* **37**, 359 (2012).
- [24] J. Knapp, D. Heck, S. Sciutto, M. Dova, and M. Risse, Extensive air shower simulations at the highest energies, *Astroparticle Physics* **19**, 77 (2003).
- [25] T. Sato, Analytical model for estimating the zenith angle dependence of terrestrial cosmic ray fluxes, *PLOS ONE* **11**, e0160390 (2016).
- [26] T. Sato, K. Niita, N. Matsuda, S. Hashimoto, Y. Iwamoto, S. Noda, T. Ogawa, H. Iwase, H. Nakashima, T. Fukahori, K. Okumura, T. Kai, S. Chiba, T. Furuta, and L. Sihver, Particle and heavy ion transport code system, PHITS, version 2.52, *Journal of Nuclear Science and Technology* **50**, 913 (2013).
- [27] A Muon Simulation for Cosmic Ray Analysis Tasks, <https://github.com/joefowler/MuscRat.jl>.
- [28] C. Hagmann, D. Lange, and D. Wright, Cosmic-ray shower generator (CRY) for Monte Carlo transport codes, in *2007 IEEE Nuclear Science Symposium Conference Record* (IEEE, 2007) pp. 1143–1146.
- [29] N. Su, Y. Liu, L. Wang, B. Wu, and J. Cheng, A comparison of muon flux models at sea level for muon imaging and low background experiments, *Frontiers in Energy Research* **9**, 750159 (2021).
- [30] J. Fowler, L. Fortson, C. Jui, D. Kieda, R. Ong, C. Pryke, and P. Sommers, A measurement of the cosmic ray spectrum and composition at the knee, *Astroparticle Physics* **15**, 49 (2001).
- [31] R. L. Workman *et al.* (Particle Data Group), Review of Particle Physics, Chapter 34: Passage of particles through matter, *PTEP* **2022**, 083C01 (2022).
- [32] P. K. Day, H. G. LeDuc, B. A. Mazin, A. Vayonakis, and J. Zmuidzinas, A broadband superconducting detector suitable for use in large arrays, *Nature* **425**, 817 (2003).
- [33] T. Cecil, A. Miceli, L. Gades, A. Datesman, O. Quaranta, V. Yefremenko, V. Novosad, and B. Mazin, Kinetic Inductance Detectors for x-ray spectroscopy, *Physics Procedia* **37**, 697 (2012).
- [34] T. W. Cecil, L. Gades, T. Madden, Daikang Yan, and A. Miceli, Optimization of thermal kinetic inductance detectors for x-ray spectroscopy, *IEEE Transactions on Applied Superconductivity* **25**, 2400805 (2015).
- [35] G. Ulbricht, B. A. Mazin, P. Szypryt, A. B. Walter, C. Bockstiegel, and B. Bumble, Highly multiplexible thermal kinetic inductance detectors for x-ray imaging spectroscopy, *Applied Physics Letters* **106**, 251103 (2015).
- [36] K. D. Irwin, G. C. Hilton, D. A. Wollman, and J. M. Martinis, X-ray detection using a superconducting transition-edge sensor microcalorimeter with electrothermal feedback, *Applied Physics Letters* **69**, 1945 (1996).
- [37] K. D. Irwin and G. C. Hilton, Transition-Edge Sensors, in *Cryogenic Particle Detection*, Topics in Applied Physics, Vol. 99, edited by C. Enss (Springer, Berlin, Heidelberg, 2005).
- [38] J. N. Ullom and D. A. Bennett, Review of superconducting transition-edge sensors for x-ray and gamma-ray spectroscopy, *Superconductor Science and Technology* **28**, 084003 (2015).
- [39] E. M. Scott, J. Caylor, M. S. Dewey, J. Gao, C. Heikes, S. F. Hoogerheide, H. P. Mumm, J. S. Nico, J. Stevens, J. Ullom, and M. Vissers, Large-area TKIDs for charged particle detection, *Journal of Low Temperature Physics* **209**, 502 (2022).
- [40] N. R. Werthamer, Theory of the superconducting transition temperature and energy gap function of superposed metal films, *Physical Review* **132**, 2440 (1963).
- [41] J. M. Martinis, G. Hilton, K. Irwin, and D. Wollman, Calculation of T_C in a normal-superconductor bilayer using the microscopic-based Usadel theory, *Nuclear Instruments and Methods in Physics Research Section A: Accelerators, Spectrometers, Detectors and Associated Equipment* **444**, 23 (2000).
- [42] M. R. Vissers, J. Gao, M. Sandberg, S. M. Duff, D. S. Wisbey, K. D. Irwin, and D. P. Pappas, Proximity-coupled Ti/TiN multilayers for use in kinetic inductance detectors, *Applied Physics Letters* **102**, 232603 (2013).
- [43] M. Tinkham, *Introduction to Superconductivity*, 2nd Edition (Dover, 2004).
- [44] R. D. Deslattes, E. Kessler, and P. Indelicato, X-ray transition energies: new approach to a comprehensive evaluation, *Reviews of Modern Physics* **75**, 35 (2003).
- [45] M. J. Berger, J. Hubbell, S. Seltzer, J. Chang, J. Coursey, R. Sukumar, D. Zucker, and K. Olsen, *XCOM: Photon Cross Section Database (version 1.5)*, *NIST Standard Reference Database 8*, Tech. Rep. (U.S. National Institute of Standards and Technology, 2010).
- [46] International Commission on Radiation Units and Measurements, *ICRU Report 37, Stopping Powers for Electrons and Positrons*, Tech. Rep. (ICRU, 1984).
- [47] A. P. M. Place, L. V. H. Rodgers, P. Mundada, B. M. Smitham, M. Fitzpatrick, Z. Leng, A. Premkumar, J. Bryon, A. Vrajitoarea, S. Sussman, G. Cheng, T. Madhavan, H. K. Babla, X. H. Le, Y. Gang, B. Jäck, A. Geynis, N. Yao, R. J. Cava, N. P. de Leon, and A. A. Houck, New material platform for superconducting transmon qubits with coherence times exceeding 0.3 milliseconds, *Nature Communications* **12**, 1779 (2021).

- [48] Y. Chen, D. Sank, P. O’Malley, T. White, R. Barends, B. Chiaro, J. Kelly, E. Lucero, M. Mariantoni, A. Megrant, C. Neill, A. Vainsencher, J. Wenner, Y. Yin, A. N. Cleland, and J. M. Martinis, Multiplexed dispersive readout of superconducting phase qubits, *Applied Physics Letters* **101**, 182601 (2012).
- [49] J. L. Orrell and B. Loer, Sensor-assisted fault mitigation in quantum computation, *Physical Review Applied* **16**, 024025 (2021).
- [50] J. Gao, *The Physics of Superconducting Microwave Resonators*, Ph.D. thesis, California Institute of Technology (2008).
- [51] A. E. Szymkowiak, R. L. Kelley, S. H. Moseley, and C. K. Stahle, Signal processing for microcalorimeters, *Journal of Low Temperature Physics* **93**, 281 (1993).
- [52] S. Agrawal, B. Steinbach, J. J. Bock, C. Frez, L. Minutolo, H. Nguyen, R. O’Brien, A. Turner, and A. Wandui, Strong negative electrothermal feedback in thermal kinetic inductance detectors, *Journal of Applied Physics* **130**, 10.1063/5.0064723 (2021).
- [53] J. W. Fowler, B. K. Alpert, W. B. Doriese, J. Hays-Wehle, Y.-I. Joe, K. M. Morgan, G. C. O’Neil, C. D. Reintsema, D. R. Schmidt, J. N. Ullom, and D. S. Swetz, When “optimal filtering” isn’t, *IEEE Transactions on Applied Superconductivity* **27**, 1 (2017).

Appendix A: Supplemental Material

1. Additional Figures and Tables

We include an additional table and five additional figures as online-only supplemental material. Table A.1 is analogous to Table II, showing energy-integrated event rates and power from models and measurements, but for the case of the TKID fabricated on a 1500 μm substrate.

Figure A.1 compares the gamma-ray observations made with an NaI spectrometer at multiple U.S. locations; they share the same essential spectral shape and differ mainly in intensity. Figure A.2 shows a model of the distribution of energy deposited in a silicon substrate 1500 μm thick by cosmic rays, as well as the breakdown by particle species; it is analogous to Figure 5 but for the thicker wafer. Figure A.3 compares the model of the energy deposited by cosmic rays into a 500 μm -thick silicon substrate, with and without the inclusion of a concrete ceiling 18 cm thick. It shows that the concrete attenuates the hadronic contribution to the spectrum, and has very little effect on the other contributions.

Figure A.4 shows that a simple model of power coupling from off-island events can explain the model-measurement discrepancies observed below 350(150) keV in the 1500(500) μm substrate. This coupling is not intended or wanted but must be estimated. In this model, we suppose that the TKIDs are sensitive to energy deposited not only in the 25 mm^2 TKID island, but also in a further 100 mm^2 of area from the supporting legs and the nearby regions of frame. The sensitivity in the legs is comparable to that of the island but falls rapidly with distance away from the legs. We have some information

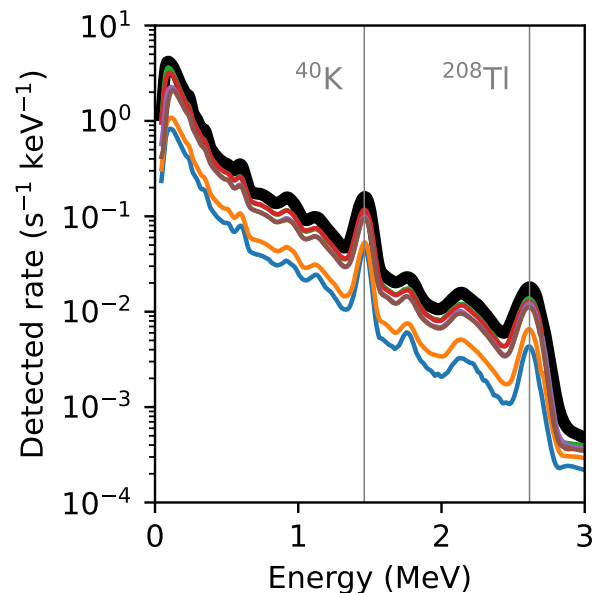


FIG. A.1. Gamma-ray background recorded by NaI scintillator spectrometer in six different labs at three buildings in two U.S. states. The spectrum with the thicker line, our reference spectrum, was measured in the same lab as the resonator measurements described in Section IV. The two energy-calibration features are indicated: 1.461 MeV gamma rays from ^{40}K and 2.615 MeV gamma rays from ^{208}Tl (in the ^{232}Th chain). Terrestrial gamma rays dominate the spectrum in the NaI detector below 2.7 MeV, while cosmic rays dominate at higher energies. Variations in the overall intensity of terrestrial gamma rays were the only notable difference among the seven spectra. The two spectra with the lowest gamma-ray activities are those measured in newer buildings.

that constrains the model. The approximate amplitude of the effect was estimated from the measurements of TKID response to LED illumination of the frame described in the main text. The size scale of the relevant frame area (100 mm^2) and the spatial distribution of the coupling was informed by modeling of Fourier’s Law thermal conduction in the island, legs, and frame. This model, though quantitative, omits ballistic phonons and has large uncertainties. We argue not that it perfectly explains the discrepancy, but that a quantitative model of the thermal coupling between the TKID inductor and the frame with plausible parameters can relieve the tension caused by the clear excess in the measured spectra over models. Future TKID designs will be undertaken with a goal of reducing this sensitivity to energy deposited close to, but not in, the island.

Figure A.5 supports our statements in Section VII that cosmic rays passing through two substrates of silicon and sapphire with equal column densities will produce nearly identical spectra, apart from lateral-area effects seen at the low-energy end of the spectra (below 100 keV). The figure shows models of cosmic rays only; the terrestrial

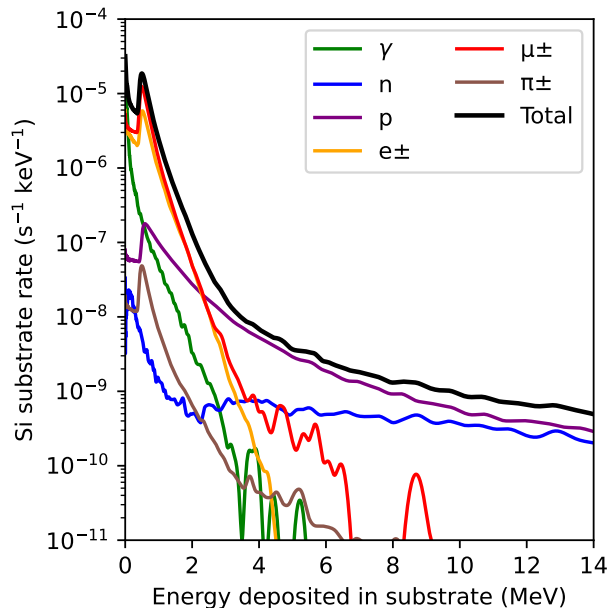


FIG. A.2. Energy deposited in a 1500 μm -thick silicon substrate by cosmic rays (models), both the total and separated by particle species. Similar to Figure 5, which shows the same spectrum components for the thinner silicon substrate (500 μm thick).

E_{\min} (keV)	Component	Event Rate (s^{-1})	Power (keV s^{-1})	Mean E (keV)
0	Gamma rays	0.066	8.8	132
0	Cosmic rays	0.0099	5.3	530
0	Model total	0.075	14.0	186
40	Gamma rays	0.038(2)	8.3(4)	221
40	Cosmic rays	0.0090(3)	5.3(1)	583
40	Model total	0.046(2)	13.6(4)	293
40	Model + frame	0.087(13)	17.4(13)	n/a
40	TKID measured	0.0778(4)	17.4(9)	223

TABLE A.1. Model and measurement of the rate of energy-absorption events, the power they deposit, and the mean energy per event, for the 1500 μm silicon substrate. All values represent integrals from E_{\min} to 20 MeV. The first three lines represent the full integral (that is, from a minimum energy of 0), relevant for instruments with high sensitivity to even the smallest background events. The next three lines represent the models integrated starting at 40 keV, where the current measurements are most reliable. These lines give the results of the gamma-ray model (Section II), the cosmic-ray model (Section III), and their sum. The Model + Frame line also adds an approximate model of the excess events that are detected in the TKID island even though the energy was deposited in the frame; this line is most appropriate for comparison to the measured rates. Uncertainties are indicated in parentheses and are dominated by systematic effects, apart from the measured TKID even rate, which is dominated by counting statistics. Equivalent results for the thinner device appear in Table II.

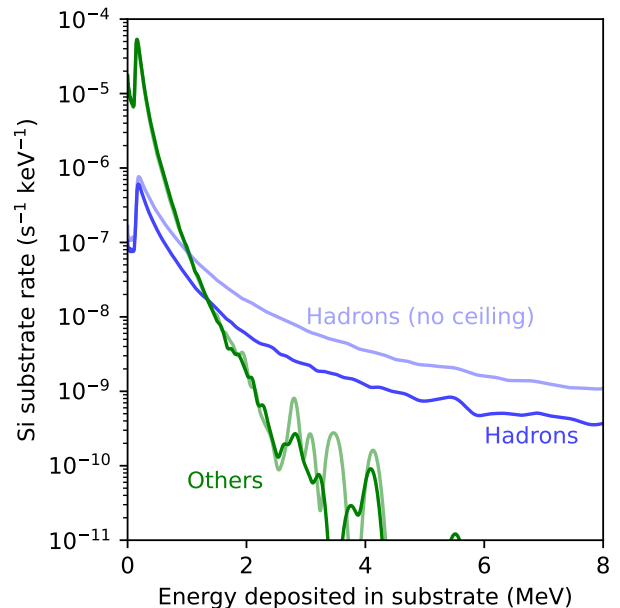


FIG. A.3. Energy deposited by cosmic-ray secondary particles into a 500 μm -thick silicon substrate (models), separated into hadronic particles (p , n , and π^{\pm}) and all others (μ^{\pm} , e^{\pm} , and γ). The heavier curves show results for the complete laboratory model, which includes a ceiling (concrete, 18 cm thick) and a proxy for the cryostat shell (aluminum, 1 cm thick). The lighter curves show the same model without ceiling or cryostat. The ceiling and shell reduce the hadronic spectrum by a factor of approximately 3 for energies $E > 2$ MeV, mainly by reducing the flux of lower-energy protons. Protons with sub-GeV energies deposit more energy per distance traveled in the silicon substrate than relativistic protons do and are responsible for the high-energy end of this spectrum [31]. The ceiling and shell reduce the spectrum of energy deposited by all other cosmic-ray particles by no more than a few percent. The analogous distributions for the thicker substrate (not shown) exhibit the same effects.

gamma-ray spectrum computed for the equivalent sapphire substrate is essentially identical to the silicon spectrum shown in Figure 3 and is therefore not shown.

2. TKID Measurements of Radiation Backgrounds

Here we describe some details of the TKID operation and readout system that we omitted from the main text.

A standard homodyne mixer is used to collect data with the TKID devices [50]. A microwave synthesizer generates a probe tone at the TKID resonant frequency (approximately 1.3 GHz for both of our devices). This signal is split, with one portion used as the reference input of an IQ (in-phase and quadrature) mixer and the other portion sent through the cryostat and TKID. This signal is amplified both cryogenically and at room temperature before reaching the RF signal input of the IQ

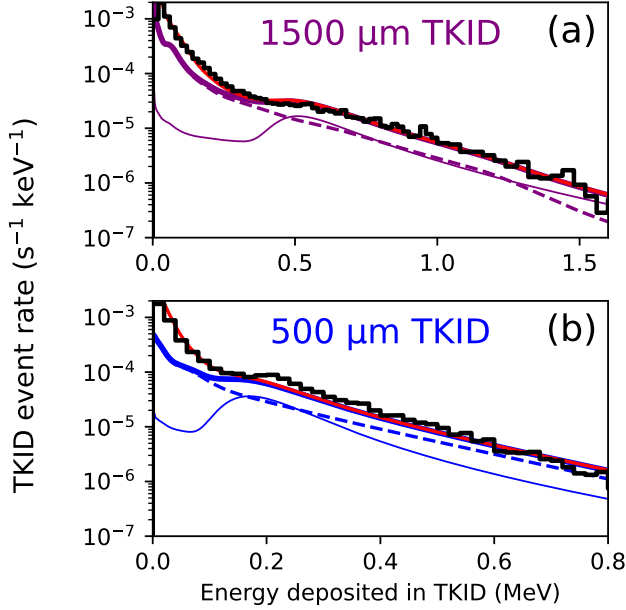


FIG. A.4. All curves are the same as shown in Figure 9, except for the addition of a red curve. It shows the total model of gamma rays and cosmic rays, *plus* the model of frame hits. The addition of a frame-hit term to the model brings the complete model into good agreement with the measurement (black histogram) below 200 (400) keV for the 500 (1500) μm substrate.

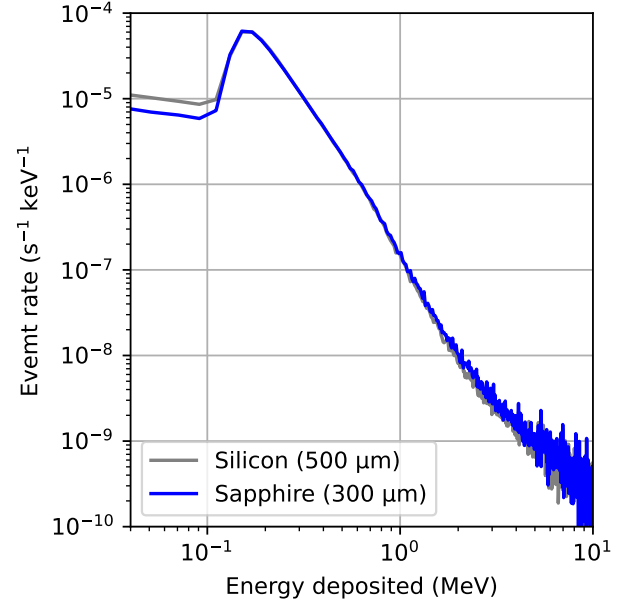


FIG. A.5. Cosmic-ray models of the spectrum of energy deposited in silicon and sapphire substrates of equal mass: 500 μm and 300 μm thick, respectively, and each 5 mm \times 5 mm. The spectra differ only at energies $E < 100$ keV, where event rates are proportional to the area of the lateral surfaces.

mixer. The I and Q outputs are digitized with a sampling rate of 1.25×10^6 samples per second. Both raw data streams are stored to disk for offline analysis.

A sweep of probe frequencies near resonance allows us to find the arc in the complex plane described by the transmission of the resonator. Characterizing all samples of the TKID measurement by their angle θ in the complex plane with respect to the center of this arc, we can replace the I and Q timestreams by a single angle. This procedure allows for more linear response and higher signal-to-noise ratio (SNR) at higher energies. Radiation events are identified in the phase-angle timestream through a level trigger: a pulse is recorded whenever four consecutive samples cross a threshold defined by three times the root-mean-square noise level.

Distinct pulse records were first analyzed by the method of “optimal filtering” [51], in which all pulses are presumed to have identical shapes and differ only in amplitude. The method takes account of the non-white nature of the intrinsic noise, and it is explicitly insensitive to slow variations in the DC level of pulse records.

In violation of the assumptions underlying optimal filtering, however, the TKID pulses exhibit a range of shapes. Specifically, after a rise time of a few μs (governed by the resonator bandwidth), pulses are found to fall with two distinct exponential time constants, typically around 60 μs and at least 240 μs . The slower time constant is consistent with conductive cooling through the TKID island’s four legs after the island has thermally equilibrated; it equals the ratio of the island’s heat capacity to the thermal conductance of the legs. The cause of the initial, faster decay time is uncertain; it may correspond to a period when the components of the TKID island are out of thermal equilibrium and/or involve electrothermal feedback from the readout tone [52]. The variation in pulse shape is primarily due to pulses having these two components in a ratio that varies, es-